

Efficient Numerical Optimization For Susceptibility Artifact Correction Of EPI-MRI

Jan Macdonald* and Lars Ruthotto†

Abstract. We present two efficient numerical methods for susceptibility artifact correction applicable in Echo Planar Imaging (EPI), an ultra fast Magnetic Resonance Imaging (MRI) technique widely used in clinical applications. Both methods address a major practical drawback of EPI, the so-called susceptibility artifacts, which consist of geometrical transformations and intensity modulations. We consider a tailored variational image registration problem that is based on a physical distortion model and aims at minimizing the distance of two oppositely distorted images subject to invertibility constraints. We follow a discretize-then-optimize approach and present a novel face-staggered discretization yielding a separable structure in the discretized distance function and the invertibility constraints. The presence of a smoothness regularizer renders the overall optimization problem non-separable, but we present two optimization schemes that exploit the partial separability. First, we derive a block-Jacobi preconditioner to be used in a Gauss-Newton-PCG method. Second, we consider a splitting of the separable and non-separable part and solve the resulting problem using the Alternating Direction Method of Multipliers (ADMM). We provide a detailed convergence proof for ADMM for this non-convex optimization problem. Both schemes are of essentially linear complexity and are suitable for parallel computing. A considerable advantage of the proposed schemes over established methods is the reduced time-to-solution. In our numerical experiment using high-resolution 3D imaging data, our parallel implementation of the ADMM method solves a 3D problem with more than 5 million degrees of freedom in less than 50 seconds on a standard laptop, which is a considerable improvement over existing methods.

Key words. Numerical Optimization, Image Registration, Echo Planar Imaging (EPI), Magnetic Resonance Imaging (MRI), Alternating Direction Method of Multipliers (ADMM), Preconditioning.

AMS subject classifications. 65K10, 92C55, 94A08.

1. Introduction. Echo-Planar-Imaging (EPI) is an ultra fast Magnetic Resonance Imaging (MRI) technique that is widely used in medical imaging applications [33]. For example, EPI is used in the neuroscience to accelerate the acquisition of Diffusion Tensor Images (DTI) [22] or intra-operatively to guide surgery [6]. While offering a substantial reduction of scan time, a drawback of EPI is its high sensitivity to small inhomogeneities of the local magnetic field. In practical applications the magnetic field is perturbed inevitably by susceptibility variations of the object being imaged. The strength of the inhomogeneity is correlated with the strength of the external magnetic field [7] and, thus, correcting for these artifacts becomes increasingly relevant for high-resolution MRI.

A physical model for distortions caused by susceptibility variations was derived in [5]. It was shown that the distortion consists of two components: a geometric displacement and a modulation of image intensities. It is important to note that for EPI-MRI the displacement is practically limited to a fixed and a priori known direction, the so-called *phase encoding*

*Technische Universität Berlin, Germany (macdonald@math.tu-berlin.de) and Emory University, Atlanta, GA, USA.

†Emory University, Atlanta, GA, USA (lruthotto@emory.edu, corresponding author). The research of this author was in part supported by National Science Foundation (NSF) Grant DMS-1522599.

direction. Distortions in the other directions (frequency encoding and slice selection direction) are negligible. It is this particular structure that we exploit in this work to obtain a partially separable objective function and efficient optimization schemes. The intensity modulation is given by the Jacobian determinant of the geometric transformation and ensures mass-preservation under the assumption that the Jacobian determinant is strictly positive almost everywhere. As mentioned in [5] this property needs to be ensured by judicious choice of the measurement parameters.

In recent years many approaches for susceptibility artifact correction were proposed; see, e.g., [17] for an extensive overview. Most of them employ the physical distortion model in [5], and fall into one of two categories. One approach is to obtain a *field map*, which is an estimate of the field inhomogeneity, from a reference scan and apply the physical model for susceptibility artifacts [20, 21]. Alternatively, the field map can be estimated using an additional EPI image with reversed phase-encoding gradients and thus opposite deformations. The estimation problem can be phrased as a nonlinear image registration problem as originally proposed in [5]. This approach, commonly referred to as *reversed gradient* method, is taken in the following.

There are several numerical implementations of the reversed gradient method, for example, [19, 30, 28, 17, 32, 1]. Given the two images, the goal is to estimate the field inhomogeneity such that the resulting deformations render both images as similar as possible to one another. Recently, several studies have shown the (often superior with respect to the field map approaches) quality of reversed gradient approaches, e.g., in Arterial Spin Labeling (ASL) [23], quantitative MRI [18], and perfusion weighted MRI [35].

Despite the increasing popularity of reversed gradient methods, relatively little attention has been paid to their efficient numerical implementation. Although the methods in [19, 30, 28, 17, 32, 1] are all based on the same physical distortion model, they employ different discretizations and optimization strategies. Hessian-based minimization schemes are used in [30, 28, 17, 32, 1]. As to be expected, the computationally most expensive step in these iterative approaches is computing the search direction, which requires approximately solving a linear system. An often neglected aspect is the impact of the chosen discretization on the complexity of this step. As we show in this work, a careful numerical discretization that is motivated by the physical distortion model can be exploited to substantially reduce the computational cost of this step.

In this paper, we present and compare two novel fast and scalable numerical optimization schemes that accelerate reversed gradient based susceptibility artifact correction. Similar to [30, 28, 17], we consider a variational formulation consisting of a distance functional and a regularization functional that improves robustness against noise. We use a discretize-then-optimize paradigm and follow the general guidelines described in [25]. In contrast to existing works, we derive a face-staggered discretization that exploits the fact that, in EPI correction, displacements are practically limited along one a priori known direction. We show that this discretization leads to a separable structure of the discrete distance function, which results in a block-diagonal Hessian, whereas the smoothness regularizer yields global coupling but has exploitable structure. We propose two approaches to exploit this structure for fast numerical optimization: First, we construct a parallel block-Jacobi preconditioner for a Gauss-Newton method. Second, we derive a completely parallelizable algorithm that aims at minimizing the

non-convex objective function using the framework of the Alternating Direction Method of Multipliers (ADMM) [2].

The complexity of the first method is linear in the number of faces in the computational mesh. The complexity of the second method is essentially linear, however, using ADMM the problem decouples into small-dimensional subproblems that can be solved efficiently and in parallel. As to be expected and shown in our experiments, this comes at the cost of an increased number of iterations and therefore the choice of method depends on the computational platform employed.

Our proposed schemes exploit the specific structure of the distortion model in EPI-MRI, where displacements due to susceptibility artifacts only occur in one spatial dimension. In contrast to that, displacements can occur in all spatial dimensions in general image registration problems. This is why the numerical techniques in this paper differ from existing efficient solvers for general image registration problems, such as, e.g. [4, 13, 36, 24].

The paper is organized as follows. Section 2 introduces the forward and inverse problem of susceptibility artifact correction. Section 3 describes the discretization using a face-staggered grid for the displacement. Section 4 describes the optimization methods. Section 5 outlines the potential of the method using real-life data. Finally, section 6 concludes the paper.

2. Mathematical Formulation. In this section, we briefly review the physical distortion model derived in [5] and the variational formulation of EPI susceptibility artifact correction also used in [30, 28]. For clarity of presentation, we limit the discussion to the three-dimensional case, which is most relevant for our applications.

Let us first derive the forward problem. Let $\Omega \subset \mathbb{R}^3$ be a rectangular domain of interest, let $v \in \mathbb{R}^3$ denote the phase-encoding direction, and let the magnitude of the field inhomogeneity at a point $x \in \Omega$ be $b(x)$, where in the forward problem $b : \Omega \rightarrow \mathbb{R}$ is assumed to be known. As derived in [5], the distorted measurement $\mathcal{I}_v : \mathbb{R}^3 \rightarrow \mathbb{R}$ and the undistorted image $\mathcal{I} : \mathbb{R}^3 \rightarrow \mathbb{R}$ satisfy

$$(1) \quad \mathcal{I}(x) = \mathcal{I}_v(x + b(x)v) \cdot \det \nabla(x + b(x)v) = \mathcal{I}_v(x + b(x)v) \cdot (1 + v^\top \nabla b(x)),$$

where $\det \nabla(x + b(x)v)$ denotes the Jacobian determinant of the transformation $x + b(x)v$. As in [25] we assume that the images are continuously differentiable and compactly supported in Ω . Note that the Jacobian determinant simplifies to a directional derivative since displacements are limited along one line. Similarly, let \mathcal{I}_{-v} denote a second image acquired with phase-encoding direction $-v$ but otherwise unchanged imaging parameters. Using the physical distortion model (1), we have

$$(2) \quad \mathcal{I}(x) = \mathcal{I}_v(x + b(x)v) \cdot (1 + v^\top \nabla b(x)) = \mathcal{I}_{-v}(x - b(x)v) \cdot (1 - v^\top \nabla b(x)).$$

In the inverse problem, both the inhomogeneity b and the undistorted image \mathcal{I} are unknown. However, given two images \mathcal{I}_v and \mathcal{I}_{-v} acquired with phase-encoding directions v and $-v$, respectively, the goal is to estimate b such that the second equality in (2) holds approximately. Commonly a simple L^2 distance term is used, i.e.,

$$(3) \quad \mathcal{D}(b) = \frac{1}{2} \int_{\Omega} \left(\mathcal{I}_v(x + b(x)v) \cdot (1 + v^\top \nabla b(x)) - \mathcal{I}_{-v}(x - b(x)v) \cdot (1 - v^\top \nabla b(x)) \right)^2 dx.$$

Minimizing the distance term alone is an ill-posed problem and thus regularization is added; see [30, 28, 17]. In [7], methods for computing the field inhomogeneity b from susceptibility properties of the brain are developed. In this work it is shown that the field inhomogeneity should be in the Sobolev space $H^1(\Omega)$ and thus, we consider the smoothness regularizer

$$(4) \quad \mathcal{S}(b) = \frac{1}{2} \int_{\Omega} \|\nabla b(x)\|^2 dx.$$

It is important to note that the physical distortion model (1) only holds if the Jacobian determinants for both phase encoding directions are strictly positive for almost all $x \in \Omega$; see [5]. Therefore, as firstly suggested in [30, 28], we impose a constraint on the Jacobian determinant

$$(5) \quad -1 \leq v^\top \nabla b(x) \leq 1 \quad \text{for almost all } x \in \Omega.$$

As also discussed [29, Sec. 3], we restrict the set of feasible field inhomogeneities to a closed ball \mathcal{B} with respect to the L^∞ -norm whose radius depends only on the diameter of Ω . To this end, note that both the distance and the regularization functional vanish for any large enough constant field inhomogeneity b , due to the fact that \mathcal{I}_v and \mathcal{I}_{-v} are supported within the bounded set Ω . However, these global minimizers of $\mathcal{D}(b)$ and $\mathcal{S}(b)$ would be implausible in practical applications. This leads to the variational problem

$$(6) \quad \min_{b \in \mathcal{B}} \{ \mathcal{J}(b) = \mathcal{D}(b) + \alpha \mathcal{S}(b) \} \quad \text{subject to } -1 \leq v^\top \nabla b(x) \leq 1, \quad \forall x \in \Omega,$$

where the parameter $\alpha > 0$ balances between minimizing the distance and the regularity of the solution. There is no general rule for choosing an “optimal” regularization parameter especially for nonlinear inverse problems, however, several criteria such as generalized cross validation [11, 12], L-curve [14], or discrepancy principle [37] are commonly used. In this paper, we assume that α is chosen by the user and in our numerical experiments we show the robustness of the proposed optimization with respect to the choice of α ; see section 5. Following the guidelines in [25] we first discretize the variational problem, see section 3, and then discuss numerical methods for solving the discrete optimization problem in section 4.

3. Discretization. In this section, we derive a face-staggered discretization of the variational problem (6) that leads to a separable structure of the discretized distance function.

Our notation follows the general guidelines in [25]. For ease of presentation, we consider a rectangular domain $\Omega = (0, 1) \times (0, 1) \times (0, 1) \subset \mathbb{R}^3$ and assume that the phase encoding direction and thus the direction of the distortion is aligned with the first coordinate axis. In other words, we assume $v = e_1$, where e_1 is the first unit vector. In our experience, this is not a practical limitation since image data can be adequately rearranged. To simplify our notation, we assume that Ω is divided into m^3 voxels with edge length $h = 1/m$ in all three coordinate directions. Our implementation supports arbitrary numbers of voxels and anisotropic voxel sizes. The images \mathcal{I}_v and \mathcal{I}_{-v} are assumed to be compactly supported and continuously differentiable functions. In practice, a continuous image model is built from discrete data by using interpolation; see [25, Sec. 3] for details.

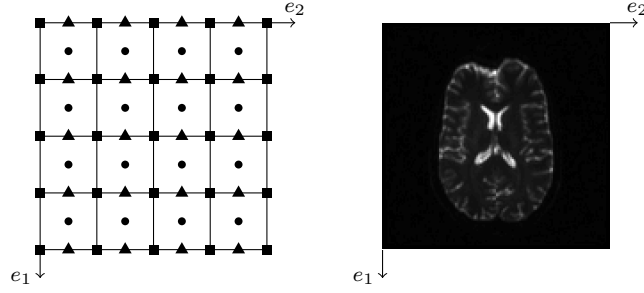


Figure 1. Cell-centered grid (circles), nodal grid (squares), and e_1 -staggered grid (triangles) on a 2-dimensional box-domain with 4×4 voxels (left). Example of a real-life deformed image (right). Data is courtesy of Harald Kugel, University Hospital Münster, Germany, cf. [section 5](#).

To obtain a separable structure of the discrete distance term, we discretize the field inhomogeneity, b , by a vector $\mathbf{b} \in \mathbb{R}^{(m+1)m^2}$ on the x_1 -faces of a regular grid as visualized in [Figure 1](#). For brevity, we denote the number of x_1 -faces by $n = (m+1)m^2$. Clearly, the elements of the vector \mathbf{b} can be accessed using linear indices or sub indices

$$\mathbf{b}_{ijk} = b((i-1)h, (j-0.5)h, (k-0.5)h), \quad \text{for } i = 1, \dots, m+1 \quad \text{and } j, k = 1, \dots, m.$$

The restriction of the field inhomogeneities b to the L^∞ -ball \mathcal{B} is discretized by restricting \mathbf{b} to a symmetric closed box $\Sigma \subseteq \mathbb{R}^n$ with edge length $2 \cdot \text{diam}(\Omega)$ around the origin. In our numerical experiments, it was not necessary to enforce this constraint. The distance functional [\(3\)](#) is approximated by a midpoint rule. To this end, the geometric transformation and the intensity modulation in [\(1\)](#) are approximated in the cell-centers by simple averaging and short finite differences, respectively. To compute the field inhomogeneity in the cell-centers given an e_1 -staggered discretization, we use the averaging matrix

$$\mathbf{A}_1 = \mathbf{I}(m^2) \otimes \tilde{\mathbf{A}}_1, \quad \tilde{\mathbf{A}}_1 = \frac{1}{2} \begin{pmatrix} 1 & 1 & & 0 \\ & \ddots & \ddots & \\ 0 & & 1 & 1 \end{pmatrix} \in \mathbb{R}^{m \times m+1},$$

where \otimes denotes the Kronecker product of two matrices and $\mathbf{I}(k)$ denotes the identity matrix of size $k \times k$. From that we obtain the discretized displacement in e_1 -direction using

$$(7) \quad \mathbf{A} = \begin{pmatrix} \mathbf{A}_1 \\ \mathbf{0} \\ \mathbf{0} \end{pmatrix} \in \mathbb{R}^{3m^3 \times n},$$

where $\mathbf{0} \in \mathbb{R}^{m^3 \times n}$ is a matrix of all zeroes.

Similarly, we discretize the first partial differential operator using short finite differences matrices

$$(8) \quad \mathbf{D}_1 = \mathbf{I}(m^2) \otimes \tilde{\mathbf{D}}(m+1, h), \quad \text{where } \tilde{\mathbf{D}}(m, h) = \frac{1}{h} \begin{pmatrix} -1 & 1 & & 0 \\ & \ddots & \ddots & \\ 0 & & -1 & 1 \end{pmatrix} \in \mathbb{R}^{(m-1) \times m}.$$

Combining (7) and (8) the distance functional (3) is approximated by

$$(9) \quad D(\mathbf{b}) = \frac{h^3}{2} \|\mathcal{I}_v(\mathbf{x} + \mathbf{A}\mathbf{b}) \odot (\mathbf{e} + \mathbf{D}_1\mathbf{b}) - \mathcal{I}_{-v}(\mathbf{x} - \mathbf{A}\mathbf{b}) \odot (\mathbf{e} - \mathbf{D}_1\mathbf{b})\|^2,$$

where \mathbf{x} are the cell-centers of a uniform grid, $\mathcal{I}_{\pm v}(\mathbf{x} \pm \mathbf{A}\mathbf{b})$ denote vectors of the image intensities at the shifted grid points, \odot denotes the component-wise Hadamard product, and $\mathbf{e} \in \mathbb{R}^{m^3}$ is a vector of all ones.

Similarly, we approximate the regularization functional (4) by

$$(10) \quad S(\mathbf{b}) = \frac{h^3}{2} \left(\|\mathbf{D}_1\mathbf{b}\|^2 + \|\mathbf{D}_2\mathbf{b}\|^2 + \|\mathbf{D}_3\mathbf{b}\|^2 \right),$$

where the discrete partial derivative operators are

$$(11) \quad \mathbf{D}_2 = \mathbf{I}(m) \otimes \tilde{\mathbf{D}}(m, h) \otimes \mathbf{I}(m+1) \quad \text{and} \quad \mathbf{D}_3 = \tilde{\mathbf{D}}(m, h) \otimes \mathbf{I}(m \cdot (m+1)).$$

Using (8) to discretize the constraint and combining (9) and (10), we obtain the finite-dimensional optimization problem

$$(12) \quad \min_{\mathbf{b} \in \Sigma} \{J(\mathbf{b}) = D(\mathbf{b}) + \alpha S(\mathbf{b})\} \quad \text{subject to} \quad -1 \leq \mathbf{D}_1\mathbf{b} \leq 1.$$

All components of the optimization problem are smooth, the regularizer is a convex quadratic, the constraints are convex, however, the distance function is in general non-convex. The non-convexity is addressed using a multilevel strategy; see subsection 4.4. In this paper, we consider two approaches for incorporating the linear inequality constraints. First, we consider augmenting the objective function by the penalty term introduced in [28]

$$(13) \quad P(\mathbf{b}) = \beta h^3 \mathbf{e}^\top \varphi(\mathbf{D}_1\mathbf{b}), \quad \varphi: \mathbb{R} \rightarrow \mathbb{R}: x \mapsto \begin{cases} \frac{x^4}{(1-x^2)} & , \text{ if } -1 \leq x \leq 1 \\ \infty & , \text{ else} \end{cases},$$

where $\beta > 0$ is a penalty parameter and φ is applied component-wise. The penalty function can be interpreted as a simplification of the volume term of the hyperelastic regularization function in [3] for transformations that are limited along one spatial directions. As also proposed in [28] we use an inexact Gauss-Newton method for solving the resulting smooth and box-constrained optimization problem

$$(14) \quad \min_{\mathbf{b} \in \Sigma} \{J_{\text{GN}}(\mathbf{b}) = D(\mathbf{b}) + \alpha S(\mathbf{b}) + P(\mathbf{b})\}.$$

In contrast to [28] we exploit the separable structure of the data term and the penalty to develop an effective and efficient preconditioner. Second, we exploit the separable structure of the distance term and the constraints in (12) and derive an efficient implementation of a Sequential Quadratic Programming (SQP) method. Both approaches are described in more detail in section 4.

In preparation for efficient, Hessian-based optimization, we quickly derive the gradients and approximate Hessians of the discretized distance, regularizer, and penalty term. Let us denote the residual of the distance term (9) by

$$\mathbf{r}(\mathbf{b}) = \mathcal{I}_v(\mathbf{x} + \mathbf{A}\mathbf{b}) \odot (\mathbf{e} + \mathbf{D}_1\mathbf{b}) - \mathcal{I}_{-v}(\mathbf{x} - \mathbf{A}\mathbf{b}) \odot (\mathbf{e} - \mathbf{D}_1\mathbf{b}).$$

Then, denoting the Jacobian matrix of the residual for a fixed \mathbf{b} by $\mathbf{J}_r(\mathbf{b}) \in \mathbb{R}^{m^3 \times n}$, we obtain the gradient and Gauss-Newton approximation to the Hessian as

$$\nabla D(\mathbf{b}) = h^3 \mathbf{J}_r(\mathbf{b})^\top \mathbf{r}(\mathbf{b}) \quad \text{and} \quad \nabla^2 D(\mathbf{b}) \approx \mathbf{H}_D(\mathbf{b}) = h^3 \mathbf{J}_r(\mathbf{b})^\top \mathbf{J}_r(\mathbf{b}).$$

The Jacobian of the residual, is given by

$$\begin{aligned} \mathbf{J}_r(\mathbf{b}) = & \text{diag}(\partial_1 \mathcal{I}_v(\mathbf{x} + \mathbf{A}\mathbf{b}) \odot (\mathbf{e} + \mathbf{D}_1 \mathbf{b})) \mathbf{A}_1 + \text{diag}(\mathcal{I}_v(\mathbf{x} + \mathbf{A}\mathbf{b})) \mathbf{D}_1 \\ & + \text{diag}(\partial_1 \mathcal{I}_{-v}(\mathbf{x} - \mathbf{A}\mathbf{b}) \odot (\mathbf{e} - \mathbf{D}_1 \mathbf{b})) \mathbf{A}_1 + \text{diag}(\mathcal{I}_{-v}(\mathbf{x} - \mathbf{A}\mathbf{b})) \mathbf{D}_1, \end{aligned}$$

where $\partial_1 \mathcal{I}_{\pm v}(\mathbf{x} \pm \mathbf{A}\mathbf{b})$ denote vectors of the first partial derivatives of the images evaluated at the shifted grid points and $\text{diag}(\mathbf{v}) \in \mathbb{R}^{n \times n}$ is a diagonal matrix with diagonal entries given by the vector $\mathbf{v} \in \mathbb{R}^n$.

Unlike the distance function, the regularizer introduces coupling along all dimensions. The Hessian and the gradient of the regularization function (10) are

$$\nabla^2 S = h^3 \left(\mathbf{D}_1^\top \mathbf{D}_1 + \mathbf{D}_2^\top \mathbf{D}_2 + \mathbf{D}_3^\top \mathbf{D}_3 \right) \quad \text{and} \quad \nabla S(\mathbf{b}) = \nabla^2 S \mathbf{b}.$$

It is important to note though that $\nabla^2 S$ is of Block-Toeplitz-Toeplitz-Block (BTTB) structure. Finally, the gradient and Hessian of the penalty term (13) are

$$\nabla P(\mathbf{b}) = \beta h^3 \mathbf{D}_1 \varphi'(\mathbf{D}_1 \mathbf{b}) \quad \text{and} \quad \nabla^2 P(\mathbf{b}) = \beta h^3 \mathbf{D}_1^\top \text{diag}(\varphi''(\mathbf{D}_1 \mathbf{b})) \mathbf{D}_1,$$

for feasible \mathbf{b} , i.e., $-1 \leq \mathbf{D}_1 \mathbf{b} \leq 1$. Here, the functions

$$(15) \quad \varphi'(x) = \frac{4x^3 - 2x^5}{(1-x^2)^2} \quad \text{and} \quad \varphi''(x) = \frac{2x^2(x^4 - 3x^2 + 6)}{(1-x^2)^3}, \quad x \in [-1, 1]$$

are applied component-wise. Combining the above derivations, the gradients and approximated Hessians of the discrete objective functions are

$$(16) \quad \nabla J(\mathbf{b}) = \nabla D(\mathbf{b}) + \alpha \nabla S(\mathbf{b}) \quad \text{and} \quad \mathbf{H}_J(\mathbf{b}) = \mathbf{H}_D(\mathbf{b}) + \alpha \nabla^2 S + \gamma \mathbf{I}(n)$$

and

$$(17) \quad \nabla J_{\text{GN}}(\mathbf{b}) = \nabla J(\mathbf{b}) + \nabla P(\mathbf{b}) \quad \text{and} \quad \mathbf{H}_{J_{\text{GN}}}(\mathbf{b}) = \mathbf{H}_J(\mathbf{b}) + \nabla^2 P(\mathbf{b})$$

respectively, where $\gamma > 0$ ensures that the approximate Hessians are symmetric positive definite. In our numerical experiments, we choose $\gamma = 10^{-3}$.

The optimization methods presented in the following section exploit the sparsity structure of the Hessian matrix. Due to the choice of the average operator \mathbf{A} and the short finite difference operator \mathbf{D}_1 , the Hessian of the distance function has a block-diagonal structure with tridiagonal blocks of size $(m+1) \times (m+1)$; see also Figure 2. Thus, minimizing the distance term would decouple into several smaller optimization problems. The Hessian of the regularizer, $\nabla^2 S$, is a discrete version of the negative Laplacian on Ω with homogeneous Neumann boundary conditions and has a banded structure. The term $\mathbf{D}_1^\top \mathbf{D}_1$ has the same

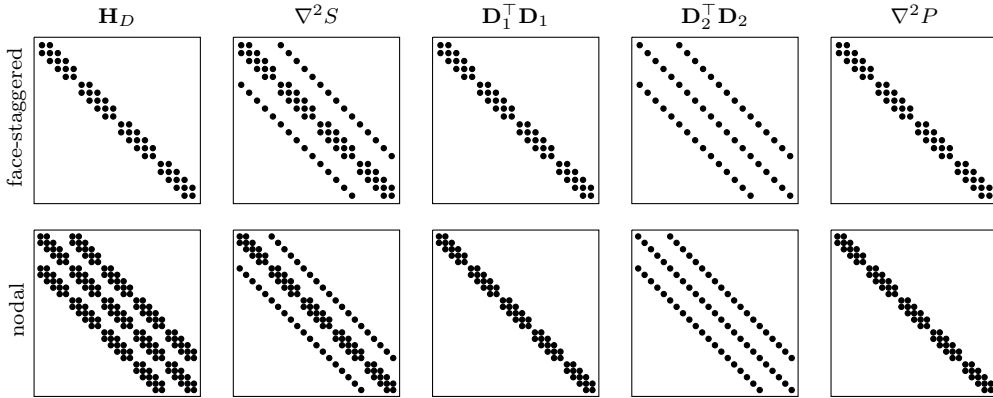


Figure 2. Sparsity patterns of the (approximated) Hessians of the distance function, smoothness regularizer, its first and second term, and of the Hessian of the penalty function (from left to right) for the e_1 -staggered discretization (top row) and the nodal discretization used in [30, 28] (bottom row) for the 4×4 example shown in Figure 1. Note that the Hessian of the distance term, the first term of the regularizer and the Hessian of the penalty function are separable with respect to image columns for the face-staggered discretization. Coupling is only introduced by the second term of the Hessian of the smoothness regularizer.

block-diagonal structure with tridiagonal blocks of size $(m+1) \times (m+1)$ as $\nabla^2 D$. So the coupling introduced by the regularizer comes from the terms $\mathbf{D}_2^\top \mathbf{D}_2$ and $\mathbf{D}_3^\top \mathbf{D}_3$ only. The Hessian of the penalty, $\nabla^2 P$, has the same block-diagonal structure with tridiagonal blocks as $\nabla^2 D$. Figures 1 and 2 show a comparison of the proposed face-staggered discretization and the nodal discretization used in [30, 28] as well as the resulting sparsity patterns of the terms of the approximate Hessians \mathbf{H}_J and $\mathbf{H}_{J_{\text{GN}}}$.

4. Numerical Optimization. In this section, we propose two efficient iterative methods for solving the discretized constrained optimization problem (12). Both methods exploit the separability achieved by the face-staggered discretization and are scalable in the sense that their complexity grows *linearly* or *essentially linearly* with the number of unknowns in the discrete optimization problem. In subsection 4.1 we derive an inexact Gauss-Newton method with a novel parallel block-Jacobi preconditioner and prove its convergence. In subsection 4.2 we use the Alternating Direction Method of Multipliers (ADMM) to decouple the optimization into small subproblems that can be solved efficiently and in parallel. Traditional convergence results for ADMM such as in [2] do not hold here, due to the non-convexity of the objective function $J(\mathbf{b})$. Thus, in subsection 4.3 we prove convergence results for ADMM specific to problem (12). Finally, in subsection 4.4 we describe the coarse-to-fine multilevel strategy used in our experiments. Throughout this section, we denote the iteration counter by superscripts.

4.1. Gauss-Newton-PCG. The first approach is an inexact Gauss-Newton method (GN-PCG) for solving the penalty formulation (14). Starting with $\mathbf{b}^0 \equiv 0$, the k -th step of the iteration reads

$$(18) \quad \mathbf{b}^{k+1} = \mathbf{b}^k - \lambda^k \mathbf{H}_{J_{\text{GN}}}(\mathbf{b}^k)^{-1} \nabla J_{\text{GN}}(\mathbf{b}^k),$$

where $\mathbf{H}_{J_{\text{GN}}}(\mathbf{b}^k)$ and $\nabla J_{\text{GN}}(\mathbf{b}^k)$ are computed according to (17) and λ^k is a step-size satisfying the Wolfe conditions [26, Ch. 3]. This step-size choice guarantees the convergence of

the GN-PCG method to a stationary point even if the linear system in (18) is solved only approximately. More precisely, instead of (18) we consider the iterative scheme

$$(19) \quad \mathbf{b}^{k+1} = \mathbf{b}^k + \lambda^k \mathbf{d}^k$$

with λ^k chosen as before and step directions \mathbf{d}^k satisfying

$$(20) \quad \left\| \nabla J_{\text{GN}}(\mathbf{b}^k) + \mathbf{H}_{J_{\text{GN}}}(\mathbf{b}^k) \mathbf{d}^k \right\| \leq \eta \left\| \nabla J_{\text{GN}}(\mathbf{b}^k) \right\|,$$

where $0 < \eta < 1$ is also known as a forcing parameter and controls the accuracy of the PCG method. In our numerical experiments, we choose $\eta = 10^{-1}$.

Theorem 1. *For any feasible starting guess \mathbf{b}^0 with $J_{\text{GN}}(\mathbf{b}^0) < \infty$ and sufficiently small η , the iterative scheme (19) converges to a stationary point of $J_{\text{GN}}(\mathbf{b})$, i.e., $\left\| \nabla J_{\text{GN}}(\mathbf{b}^k) \right\| \rightarrow 0$ as $k \rightarrow \infty$.*

The proof of the above result is divided into two Lemmas. First, we verify that the assumptions of Zoutendijk's result are satisfied for our problem; see, e.g., [26, Thm. 3.2].

Lemma 2. *Let \mathbf{b}^0 be a starting guess with $J_{\text{GN}}(\mathbf{b}^0) < \infty$ and let $S_0 \subseteq \Sigma$ be the sub-level set*

$$S_0 = \{ \mathbf{b} \in \Sigma : J_{\text{GN}}(\mathbf{b}) \leq J_{\text{GN}}(\mathbf{b}^0) \}.$$

Then, the objective function in (14) satisfies

1. $J_{\text{GN}}(\mathbf{b}) \geq 0$ for all $\mathbf{b} \in \Sigma$.
2. J_{GN} is continuously differentiable on a neighborhood S_1 of S_0 .
3. ∇J_{GN} is Lipschitz continuous on S_1 .

Proof. The above properties follow immediately, since $S_0 \subseteq \Sigma$ is compact and J_{GN} is twice continuously differentiable on any open set S with $S \subseteq \{ \mathbf{b} \in \mathbb{R}^n : J_{\text{GN}}(\mathbf{b}) < \infty \}$. Choosing open neighborhoods S_1 and $\overline{S_2}$ such that $S_0 \subseteq S_1 \subseteq \overline{S_1} \subseteq S_2 \subseteq \{ \mathbf{b} \in \mathbb{R}^n : J_{\text{GN}}(\mathbf{b}) < \infty \}$ where S_1 is bounded and $\overline{S_1}$ denotes its closure proves the claim. ■

Due to the above lemma and the fact that λ^k and \mathbf{d}^k satisfy the Wolfe conditions, Zoutendijk's result holds and in particular

$$\sum_{k \geq 0} \cos^2 \theta_k \left\| \nabla J_{\text{GN}}(\mathbf{b}^k) \right\|^2 < \infty,$$

where θ_k denotes the angle between $-\nabla J_{\text{GN}}(\mathbf{b}^k)$ and \mathbf{d}^k . To show that $\nabla J_{\text{GN}}(\mathbf{b}^k) \rightarrow 0$ as $k \rightarrow \infty$, we show in the following that $\cos \theta_k$ is uniformly bounded away from zero.

Lemma 3. *For all k , \mathbf{d}^k is a descent direction and there exists $M > 0$ such that*

$$\cos \theta_k \geq M > 0.$$

Proof. First, we show that there exist universal constants $0 < M_1 \leq M_2 < \infty$ such that

$$(21) \quad M_1 \leq \mathbf{x}^\top \mathbf{H}_{J_{\text{GN}}}(\mathbf{b}) \mathbf{x} \leq M_2, \quad \text{for all } \mathbf{x} \in \mathcal{B}_{\|\cdot\|} \quad \text{and} \quad \mathbf{b} \in S_0,$$

where S_0 is defined in Lemma 2 and

$$\mathcal{B}_{\|\cdot\|} = \{ \mathbf{u} \in \mathbb{R}^n : \|\mathbf{u}\| = 1 \}.$$

Since S_0 and $\mathcal{B}_{\|\cdot\|}$ are compact and $\mathbf{b} \mapsto \mathbf{H}_{J_{\text{GN}}}(\mathbf{b})$ is continuous on S_0 , the mapping

$$(\mathbf{b}, \mathbf{x}) \mapsto \mathbf{x}^\top \mathbf{H}_{J_{\text{GN}}}(\mathbf{b}) \mathbf{x}$$

attains a global maximum, $M_2 < \infty$, and a global minimum, $M_1 \geq \gamma > 0$, on $S_0 \times \mathcal{B}_{\|\cdot\|}$. The lower bound on M_1 follows from the fact that the first three terms of $\mathbf{H}_{J_{\text{GN}}}$ are positive semi-definite and $\gamma > 0$; see (17). Combining (20) and (21) we obtain

$$\cos \theta_k = -\frac{\nabla J(\mathbf{b}^k)^\top \mathbf{d}^k}{\|\nabla J(\mathbf{b}^k)\| \|\mathbf{d}^k\|} \geq \frac{M_1 - \eta M_2}{(1 + \eta) M_2} = M > 0$$

for any $0 < \eta < \frac{M_1}{M_2}$. Finally, as in [26], the lower bound on $\cos \theta_k$ implies that \mathbf{d}^k is a descent direction. \blacksquare

Proof of Theorem 1. The previous Lemmas verify the assumptions for Zoutendijk's result and show that the angle between the negative gradient and the search direction is bounded away from 90 degrees. The first one implies

$$\sum_{k \geq 0} \cos^2 \theta_k \left\| \nabla J_{\text{GN}}(\mathbf{b}^k) \right\|^2 < \infty.$$

Since $\cos \theta_k \geq M > 0$ we see that $\nabla J_{\text{GN}}(\mathbf{b}^k) \rightarrow 0$ as $k \rightarrow \infty$. \blacksquare

As the problem size is quite large in 3D applications we use a Preconditioned Conjugate Gradient (PCG) method for approximately solving (18); see [16] for the original work on CG and, e.g., [31, Ch.9] for an introduction to preconditioning. The performance of the method depends on the spectral properties of $\mathbf{H}_{J_{\text{GN}}}$ and in particular on the clustering of its eigenvalues. It is well known that penalty and barrier methods can lead to severe ill-conditioning of the associated Hessians; see, e.g., [26, Ch. 17]. In our application, the penalty function and its derivatives (15) grow to infinity as the magnitude of the first partial derivative of the inhomogeneity approaches one by design. Thus, effective preconditioners are required when correcting highly distorted data.

We show in this paper that effective preconditioning can be achieved by exploiting the sparsity structure of $\mathbf{H}_{J_{\text{GN}}}(\mathbf{b}^k)$. To be precise, we propose using the block-Jacobi preconditioner

$$(22) \quad \mathbf{P}_{\text{block}}(\mathbf{b}^k) = \mathbf{H}_D(\mathbf{b}^k) + \alpha \left(\mathbf{D}_1^\top \mathbf{D}_1 + \mathbf{M} \right) + \nabla^2 P(\mathbf{b}^k),$$

where \mathbf{M} is the matrix containing only the diagonal of the last two terms in the Hessian of the regularizer, i.e., $\mathbf{D}_2^\top \mathbf{D}_2 + \mathbf{D}_3^\top \mathbf{D}_3$. In the following section, we compare the performance of this preconditioner to the Jacobi-preconditioner $\mathbf{P}_{\text{Jac}}(\mathbf{b}^k)$ containing only the diagonal of $\mathbf{H}_{J_{\text{GN}}}(\mathbf{b}^k)$, and the symmetric Gauss-Seidel preconditioner

$$(23) \quad \mathbf{P}_{\text{SGS}}(\mathbf{b}) = (\mathbf{L}^k + \mathbf{P}_{\text{Jac}}(\mathbf{b}^k)) \mathbf{P}_{\text{Jac}}^{-1}(\mathbf{b}^k) (\mathbf{U}^k + \mathbf{P}_{\text{Jac}}(\mathbf{b}^k)),$$

where \mathbf{L}^k and \mathbf{U}^k are the strictly lower and upper triangular part of $\mathbf{H}_{J_{\text{GN}}}(\mathbf{b}^k)$, respectively; see [31, Ch. 10] for more details.

Solving a linear system with matrix $\mathbf{P}_{\text{block}}(\mathbf{b}^k)$ can be broken down into solving m^2 linear systems of size $m+1$, which can be done in parallel. Furthermore, solving each $m+1 \times m+1$ system is of linear complexity due to its tridiagonal structure. Therefore, the computational complexity of the preconditioner grows linearly with respect to the number of x_1 -faces, i.e., $\mathcal{O}(n)$. Thus, the asymptotic complexity of $\mathbf{P}_{\text{block}}(\mathbf{b}^k)$ is the same as the one for Jacobi and Gauss-Seidel preconditioners applied to the sparse Hessian. However, the effective runtimes may vary considerably between the preconditioners, due to the degree of parallelism. While the Jacobi preconditioner requires only component-wise division and is thus the cheapest and fastest to compute, the Gauss-Seidel preconditioner is not straightforward to parallelize and therefore, in our experiments, the most costly per iteration; see section 5.

We use the criteria suggested in [25] for stopping the Gauss-Newton method. The iteration is stopped when prescribed tolerances for the relative changes in the objective function value, the iterate, and the norm of the gradient are reached, i.e., if all of the following three conditions hold

$$(24) \quad \left| J_{\text{GN}}(\mathbf{b}^{k+1}) - J_{\text{GN}}(\mathbf{b}^k) \right| \leq \epsilon_{\text{obj}} (1 + |J_{\text{GN}}(\mathbf{0})|)$$

$$(25) \quad \left\| \mathbf{b}^{k+1} - \mathbf{b}^k \right\| \leq \epsilon_{\text{iter}} \left(1 + \left\| \mathbf{b}^k \right\| \right)$$

$$(26) \quad \left\| \nabla J_{\text{GN}}(\mathbf{b}^{k+1}) \right\| \leq \epsilon_{\text{grad}} (1 + |J_{\text{GN}}(\mathbf{0})|),$$

or a maximum number of iterations is exceeded. In our later experiments the maximum number of iterations is set to 10, which is the default setting in [30]. As common in inverse problems, we solve (14) only to a relatively low accuracy. In our numerical experiments we choose $\epsilon_{\text{obj}} = 10^{-3}$, $\epsilon_{\text{iter}} = \epsilon_{\text{grad}} = 10^{-2}$.

4.2. ADMM. The second approach we consider is based on the Alternating Direction Method of Multipliers (ADMM). Originally developed in the mid 1970s, ADMM recently received a lot of attention in many data science and imaging applications; see, e.g., [9] and the recent surveys [2, 8, 10]. The key idea in our case is to split the terms of the objective function (12) that are separable with respect to columns of the images from those terms that couple across image columns. To this end, let \mathbf{z} be a new artificial variable and split the objective function J into

$$(27) \quad f(\mathbf{b}) = D(\mathbf{b}) + \frac{\alpha h^3}{2} \|\mathbf{D}_1 \mathbf{b}\|^2 \quad \text{and} \quad g(\mathbf{z}) = \frac{\alpha h^3}{2} \left(\|\mathbf{D}_2 \mathbf{z}\|^2 + \|\mathbf{D}_3 \mathbf{z}\|^2 \right).$$

Then we consider

$$(28) \quad \min_{\mathbf{b}, \mathbf{z} \in \mathbb{R}^n} \iota_C(\mathbf{b}) + f(\mathbf{b}) + g(\mathbf{z}) \quad \text{subject to} \quad \mathbf{b} = \mathbf{z},$$

where we encode the linear inequality constraints into the objective function, using the indicator function $\iota_C(\mathbf{b})$ of the compact and convex set $C = \{ \mathbf{b} \in \Sigma : -1 \leq \mathbf{D}_1 \mathbf{b} \leq 1 \}$, taking

the value 0, whenever $\mathbf{b} \in C$, and ∞ otherwise. Thus, (28) is equivalent to (12). For an augmentation parameter $\rho > 0$, whose choice is discussed below, we aim at finding a stationary point of the augmented Lagrangian of (28)

$$(29) \quad \mathcal{L}_\rho(\mathbf{b}, \mathbf{z}, \mathbf{y}) = \iota_C(\mathbf{b}) + f(\mathbf{b}) + g(\mathbf{z}) + \mathbf{y}^\top (\mathbf{b} - \mathbf{z}) + \frac{\rho h^3}{2} \|\mathbf{b} - \mathbf{z}\|^2,$$

where $\mathbf{y} \in \mathbb{R}^n$ is the Lagrange multiplier associated with the equality constraint in (28). The idea of ADMM is to update \mathbf{b} , \mathbf{z} , and \mathbf{y} in an alternating fashion

$$(30) \quad \mathbf{b}^{k+1} = \underset{\mathbf{b} \in \mathbb{R}^n}{\operatorname{argmin}} \mathcal{L}_\rho(\mathbf{b}, \mathbf{z}^k, \mathbf{y}^k),$$

$$(31) \quad \mathbf{z}^{k+1} = \underset{\mathbf{z} \in \mathbb{R}^n}{\operatorname{argmin}} \mathcal{L}_\rho(\mathbf{b}^{k+1}, \mathbf{z}, \mathbf{y}^k),$$

$$(32) \quad \mathbf{y}^{k+1} = \mathbf{y}^k + \rho h^3 (\mathbf{b}^{k+1} - \mathbf{z}^{k+1}).$$

Introducing the scaled dual variable $\mathbf{u} = \mathbf{y}/(\rho h^3)$, we obtain the following iteration

$$(33) \quad \mathbf{b}^{k+1} = \underset{\mathbf{b} \in \mathbb{R}^n}{\operatorname{argmin}} \left\{ \iota_C(\mathbf{b}) + f(\mathbf{b}) + \frac{\rho h^3}{2} \|\mathbf{b} - \mathbf{z}^k + \mathbf{u}^k\|^2 \right\},$$

$$(34) \quad \mathbf{z}^{k+1} = \underset{\mathbf{z} \in \mathbb{R}^n}{\operatorname{argmin}} \left\{ g(\mathbf{z}) + \frac{\rho h^3}{2} \|\mathbf{b}^{k+1} - \mathbf{z} + \mathbf{u}^k\|^2 \right\},$$

$$(35) \quad \mathbf{u}^{k+1} = \mathbf{u}^k + \mathbf{b}^{k+1} - \mathbf{z}^{k+1}.$$

The first subproblem, updating \mathbf{b} , is a non-convex constrained optimization problem and approximately solved using sequential quadratic programming (SQP) as described below. For the discretization derived in the previous section, this problem is separable with respect to the columns in the image and thus can be further broken down into m^2 separate steps. In each iteration of the SQP method, we form a quadratic approximation of the objective function and solve the resulting quadratic program (QP) using the active set method with Schur complement solver described in [26, Ch. 16]. The general form of the QP is

$$(36) \quad \min_{\mathbf{x}} \frac{1}{2} \mathbf{x}^\top \mathbf{G} \mathbf{x} + \mathbf{c}^\top \mathbf{x} \quad \text{subject to} \quad \mathbf{A} \mathbf{x} \geq \mathbf{d},$$

where, in our case, \mathbf{G} is the respective Hessian approximation, \mathbf{c} is the gradient, \mathbf{D}_1 and $-\mathbf{D}_1$ are stacked into \mathbf{A} , and \mathbf{d} is a vector of all negative ones. Let \mathbf{x}^k be the current iterate in this QP and I be a subset of component-indices describing the active set. Further, let \mathbf{A}_I be the matrix containing the rows of \mathbf{A} associated with active constraints and let \mathbf{d}_I be the corresponding right-hand-side. Then we obtain an update direction \mathbf{p} for \mathbf{x}^k and the Lagrange multiplier $\boldsymbol{\lambda}$ of the active constraints by solving

$$(37) \quad \begin{pmatrix} \mathbf{G} & \mathbf{A}_I^\top \\ \mathbf{A}_I & \mathbf{0} \end{pmatrix} \begin{pmatrix} \mathbf{p} \\ -\boldsymbol{\lambda} \end{pmatrix} = \begin{pmatrix} -\mathbf{c} - \mathbf{G} \mathbf{x}^k \\ \mathbf{d}_I - \mathbf{A}_I \mathbf{x}^k \end{pmatrix} =: \begin{pmatrix} \mathbf{g} \\ \mathbf{h} \end{pmatrix}$$

using the Schur complement, i.e., by setting

$$\boldsymbol{\lambda} = - \left(\mathbf{A}_I \mathbf{G}^{-1} \mathbf{A}_I^\top \right)^{-1} (\mathbf{A}_I \mathbf{G}^{-1} \mathbf{g} - \mathbf{h}) \quad \text{and} \quad \mathbf{p} = \mathbf{G}^{-1} (\mathbf{A}_I^\top \boldsymbol{\lambda} + \mathbf{g}).$$

Now three cases can occur: First, if $\mathbf{p} = \mathbf{0}$ and $\boldsymbol{\lambda} \geq \mathbf{0}$ component-wise, then \mathbf{x}^k is the global solution to (36). Second, if $\mathbf{p} = \mathbf{0}$ but some components of $\boldsymbol{\lambda}$ are negative, we remove up to one constraint with negative Lagrange multiplier per block in \mathbf{A} from the active set and repeat the above computations. Third, if $\mathbf{p} \neq \mathbf{0}$, compute a step length λ^k such that $\mathbf{x}^k + \lambda^k \mathbf{p}$ is feasible but at least one additional constraint has become active. Then all of these constraints are added to the active set. Linear independence of the active constraints is guaranteed since the partial derivative at an active voxel can be either 1 or -1 . Note that the Schur complement involves \mathbf{G}^{-1} and thus an efficient method to solve linear systems with matrix \mathbf{G} is needed. In our application, the chosen discretization allows for fast inversions.

More precisely, for the update of \mathbf{b} , we have

$$\mathbf{c} = \nabla D(\mathbf{b}^k) + \alpha h^3 \mathbf{D}_1 \mathbf{b}^k + \rho h^3 (\mathbf{b}^k - \mathbf{z}^k + \mathbf{u}^k)$$

and

$$\mathbf{G} = \mathbf{H}_D(\mathbf{b}^k) + \alpha h^3 \mathbf{D}_1^\top \mathbf{D}_1 + \rho h^3 \mathbf{I}(n),$$

which has the before mentioned block-diagonal structure with tridiagonal blocks of size $m+1$. Therefore, linear systems involving \mathbf{G} can be solved in parallel by a direct method with a linear complexity of $\mathcal{O}(n)$.

The second subproblem, updating \mathbf{z} , is an unconstrained strictly convex quadratic optimization problem with a structured, symmetric positive definite Hessian

$$\tilde{\mathbf{G}} = \alpha h^3 (\mathbf{D}_2^\top \mathbf{D}_2 + \mathbf{D}_3^\top \mathbf{D}_3) + \rho h^3 \mathbf{I}(n)$$

and has the closed form solution

$$\mathbf{z}^{k+1} = \tilde{\mathbf{G}}^{-1} (\rho h^3 (\mathbf{b}^{k+1} + \mathbf{u}^k)).$$

The matrix $\tilde{\mathbf{G}}$ can be reordered into a block-diagonal matrix with $m+1$ blocks, whose blocks are matrices of size $m^2 \times m^2$. Each block is a discretization of the negative two-dimensional Laplacian with homogeneous Neumann boundary conditions on a regular mesh and thus is a Block-Toeplitz-Toeplitz-Block (BTTB) matrix. Hence, $\tilde{\mathbf{G}}$ can be diagonalized using two-dimensional Discrete Cosine Transforms (DCT); see [15, Ch. 4]. More specifically, denote by $\mathbf{C}(m) \in \mathbb{R}^{m \times m}$ the one-dimensional DCT of size m . Then we have

$$(38) \quad \tilde{\mathbf{D}}(m, h)^\top \tilde{\mathbf{D}}(m, h) = \mathbf{C}(m)^\top \boldsymbol{\Lambda}(m, h) \mathbf{C}(m)$$

for some diagonal matrix $\boldsymbol{\Lambda}(m, h)$. Combining (11) and (38), we immediately obtain

$$(39) \quad \mathbf{D}_2^\top \mathbf{D}_2 + \mathbf{D}_3^\top \mathbf{D}_3 = \mathbf{C}^\top \boldsymbol{\Lambda} \mathbf{C}, \text{ where } \mathbf{C} = \mathbf{C}(m) \otimes \mathbf{C}(m) \otimes \mathbf{I}(m+1)$$

is the two-dimensional DCT along the e_2 - and e_3 -direction, and

$$\boldsymbol{\Lambda} = \mathbf{I}(m) \otimes \boldsymbol{\Lambda}(m, h) \otimes \mathbf{I}(m+1) + \boldsymbol{\Lambda}(m, h) \otimes \mathbf{I}(m) \otimes \mathbf{I}(m+1)$$

is a diagonal matrix that only needs to be computed once for every fixed discretization (m, h) . Finally, since \mathbf{C} is orthogonal, we obtain

$$\tilde{\mathbf{G}} = \mathbf{C}^\top (\alpha h^3 \mathbf{\Lambda} + \rho h^3 \mathbf{I}(n)) \mathbf{C}.$$

Thus, the second ADMM step, updating \mathbf{z} , requires $m + 1$ two-dimensional DCTs, which is of complexity $\mathcal{O}((m + 1)(m^2 \log m^2))$, followed by a diagonal solve, and finally $m + 1$ inverse two-dimensional DCTs. Again this is a direct solve and does not require the use of iterative methods.

For the ADMM algorithm, we use the stopping criteria proposed in [2, Sec. 3], which are also justified by our convergence analysis in [subsection 4.3](#). We stop when the norm of the primal and dual residual satisfy

$$(40) \quad \left\| \mathbf{b}^{k+1} - \mathbf{z}^{k+1} \right\| \leq \epsilon_{\text{pri}} \quad \text{and} \quad \rho h^3 \left\| \mathbf{z}^k - \mathbf{z}^{k+1} \right\| \leq \epsilon_{\text{dual}},$$

where ϵ_{pri} and ϵ_{dual} are computed exactly as (3.12) in [2] using a combination of an absolute and a relative tolerance

$$\begin{aligned} \epsilon_{\text{pri}} &= \sqrt{n} \epsilon_{\text{abs}} + \epsilon_{\text{rel}} \max \left\{ \left\| \mathbf{b}^k \right\|, \left\| \mathbf{z}^k \right\| \right\} \\ \epsilon_{\text{dual}} &= \sqrt{n} \epsilon_{\text{abs}} + \epsilon_{\text{rel}} \rho h^3 \left\| \mathbf{u}^k \right\|. \end{aligned}$$

In our numerical experiments, we choose $\epsilon_{\text{abs}} = \epsilon_{\text{rel}} = 2 \cdot 10^{-1}$.

4.3. Convergence of ADMM. It is important to stress that the first subproblem in our ADMM algorithm, (33), is non-convex and thus the traditional convergence results for ADMM do not hold. However, ADMM can be considered a local optimization method and has been successfully applied to non-convex problems in other applications; see [2, Ch.9] for some examples. Recently, convergence results have been established under some modest conditions on the functions involved; see, for example, [38]. In the following, we show convergence of ADMM for the specific problem at hand. Using the smoothness of our problem we obtain a simplified, but less general, convergence proof as compared to [38]. We first note that the functions f and g in (27) are twice continuously differentiable. Further, ∇f is Lipschitz continuous over C and ∇g is Lipschitz continuous over \mathbb{R}^n . We denote the corresponding Lipschitz constants by L_f and L_g respectively. The relation between these Lipschitz constants and the augmentation parameter, ρ , is crucial in the convergence analysis. Throughout this section we use both the unscaled ADMM formulation (30)–(32) as well as the equivalent scaled formulation (33)–(35), whichever is more convenient. Recall that $\mathbf{u}^k = \mathbf{y}^k / (\rho h^3)$ is the scaled Lagrange multiplier. The main result of this section is the following.

Theorem 4. *For each $\rho > \frac{2}{h^3} \max\{L_f, L_g\}$, the sequence of iterates $\{\mathbf{b}^k, \mathbf{z}^k, \mathbf{y}^k\}$ generated by the ADMM algorithm (30)–(32) converges subsequentially and each limit point $\{\mathbf{b}^*, \mathbf{z}^*, \mathbf{y}^*\}$ is a stationary point of the Lagrangian \mathcal{L}_ρ in (29).*

As in [38], our proof is based on the following three properties.

Theorem 5. For each $\rho > \frac{2}{h^3} \max\{L_f, L_g\}$, the sequence of iterates $\{\mathbf{b}^k, \mathbf{z}^k, \mathbf{y}^k\}$ generated by the ADMM algorithm (30)–(32) has the following properties:

(P1) The iterates $\{\mathbf{b}^k, \mathbf{z}^k, \mathbf{y}^k\}$ are well-defined and bounded, and $\{\mathcal{L}_\rho(\mathbf{b}^k, \mathbf{z}^k, \mathbf{y}^k)\}_k$ is bounded below.

(P2) The value of the Lagrangian decreases sufficiently fast, meaning there exists a constant $C_1 > 0$ such that

$$\mathcal{L}_\rho(\mathbf{b}^k, \mathbf{z}^k, \mathbf{y}^k) - \mathcal{L}_\rho(\mathbf{b}^{k+1}, \mathbf{z}^{k+1}, \mathbf{y}^{k+1}) \geq C_1 \left(\|\mathbf{b}^k - \mathbf{b}^{k+1}\|^2 + \|\mathbf{z}^k - \mathbf{z}^{k+1}\|^2 \right).$$

(P3) There exists a constant $C_2 > 0$ and subgradients $\mathbf{d}^{k+1} \in \partial \mathcal{L}_\rho(\mathbf{b}^{k+1}, \mathbf{z}^{k+1}, \mathbf{y}^{k+1})$ such that

$$\|\mathbf{d}^{k+1}\| \leq C_2 \left(\|\mathbf{b}^k - \mathbf{b}^{k+1}\| + \|\mathbf{z}^k - \mathbf{z}^{k+1}\| \right).$$

We split the proof of [Theorem 5](#) into several lemmas.

Lemma 6. For $\rho > 0$ the subproblems (33) and (34) have at least one solution for all $k \in \mathbb{N}$.

Proof. For arbitrary but fixed k , the first subproblem, the update $\mathbf{b}^k \rightarrow \mathbf{b}^{k+1}$, consists of minimizing the function

$$f(\mathbf{b}) + \frac{\rho h^3}{2} \|\mathbf{b} - \mathbf{z}^k + \mathbf{u}^k\|^2$$

over the compact and convex set C . On this set f is twice continuously differentiable, so the problem is well-defined, i.e., there exists a global solution. The second subproblem, the update $\mathbf{z}^k \rightarrow \mathbf{z}^{k+1}$, consists of minimizing

$$g(\mathbf{z}) + \frac{\rho h^3}{2} \|\mathbf{b}^{k+1} - \mathbf{z} + \mathbf{u}^k\|^2$$

over $\mathbf{z} \in \mathbb{R}^n$. This problem is well defined, since g is a convex quadratic function and $\rho > 0$, which renders the overall objective function strictly convex. Thus, there exists a unique global minimizer. ■

Next we show that the augmented Lagrangian decreases sufficiently after the first ADMM step (30).

Lemma 7. If $\rho \geq \frac{2}{h^3} L_f$, then the update $\mathbf{b}^k \rightarrow \mathbf{b}^{k+1}$ does not increase the value of the augmented Lagrangian. More precisely, for $\rho > 0$

$$\mathcal{L}_\rho(\mathbf{b}^k, \mathbf{z}^k, \mathbf{y}^k) - \mathcal{L}_\rho(\mathbf{b}^{k+1}, \mathbf{z}^k, \mathbf{y}^k) \geq \left(\frac{\rho h^3}{2} - L_f \right) \|\mathbf{b}^k - \mathbf{b}^{k+1}\|^2.$$

Proof. Denote $\mathbf{d}^{k+1} = \mathbf{y}^{k+1} + \rho h^3(\mathbf{z}^{k+1} - \mathbf{z}^k)$. From the optimality condition for (30) we

conclude that \mathbf{b}^{k+1} satisfies

$$\begin{aligned}
& \mathbf{0} \in \nabla f(\mathbf{b}^{k+1}) + \partial\iota_C(\mathbf{b}^{k+1}) + \mathbf{y}^k + \rho h^3(\mathbf{b}^{k+1} - \mathbf{z}^k) \\
\Leftrightarrow & \mathbf{0} \in \nabla f(\mathbf{b}^{k+1}) + \partial\iota_C(\mathbf{b}^{k+1}) + \mathbf{y}^{k+1} + \rho h^3(\mathbf{z}^{k+1} - \mathbf{z}^k) \\
\Leftrightarrow & -\left(\nabla f(\mathbf{b}^{k+1}) + \mathbf{y}^{k+1} + \rho h^3(\mathbf{z}^{k+1} - \mathbf{z}^k)\right) \in \partial\iota_C(\mathbf{b}^{k+1}) \\
(41) \quad \Leftrightarrow & \left(\nabla f(\mathbf{b}^{k+1}) + \mathbf{d}^{k+1}\right)^\top (\mathbf{w} - \mathbf{b}^{k+1}) \geq 0 \quad \forall \mathbf{w} \in C.
\end{aligned}$$

Here, we used that the subgradient of an indicator function of a convex set C is

$$\partial\iota_C(\mathbf{b}^{k+1}) = \left\{ \mathbf{d} \in \mathbb{R}^n : \mathbf{d}^\top (\mathbf{w} - \mathbf{b}^{k+1}) \leq 0, \forall \mathbf{w} \in C \right\},$$

see also [27, Ch. 8]. Denoting $\mathcal{L}_\rho^k = \mathcal{L}_\rho(\mathbf{b}^k, \mathbf{z}^k, \mathbf{y}^k)$ and $\mathcal{L}_\rho^{k+1} = \mathcal{L}_\rho(\mathbf{b}^{k+1}, \mathbf{z}^k, \mathbf{y}^k)$ we get

$$\begin{aligned}
\mathcal{L}_\rho^k - \mathcal{L}_\rho^{k+1} &= f(\mathbf{b}^k) - f(\mathbf{b}^{k+1}) + (\mathbf{y}^k)^\top (\mathbf{b}^k - \mathbf{b}^{k+1}) + \frac{\rho h^3}{2} \left(\|\mathbf{b}^k - \mathbf{z}^k\|^2 - \|\mathbf{b}^{k+1} - \mathbf{z}^k\|^2 \right) \\
&= f(\mathbf{b}^k) - f(\mathbf{b}^{k+1}) + (\mathbf{d}^{k+1})^\top (\mathbf{b}^k - \mathbf{b}^{k+1}) + \frac{\rho h^3}{2} \|\mathbf{b}^k - \mathbf{b}^{k+1}\|^2 \\
&= f(\mathbf{b}^k) - f(\mathbf{b}^{k+1}) - \nabla f(\mathbf{b}^{k+1})^\top (\mathbf{b}^k - \mathbf{b}^{k+1}) \\
&\quad + \left(\nabla f(\mathbf{b}^{k+1}) + \mathbf{d}^{k+1}\right)^\top (\mathbf{b}^k - \mathbf{b}^{k+1}) + \frac{\rho h^3}{2} \|\mathbf{b}^k - \mathbf{b}^{k+1}\|^2 \\
&\geq \left(\frac{\rho h^3}{2} - L_f \right) \|\mathbf{b}^k - \mathbf{b}^{k+1}\|^2,
\end{aligned}$$

where we used (41) and the Lipschitz continuity of ∇f in the last step. ■

A similar result also holds for the second ADMM step (31).

Lemma 8. *For any $\rho > 0$, the update $\mathbf{z}^k \rightarrow \mathbf{z}^{k+1}$ does not increase the value of the augmented Lagrangian. More precisely,*

$$\mathcal{L}_\rho(\mathbf{b}^{k+1}, \mathbf{z}^k, \mathbf{y}^k) - \mathcal{L}_\rho(\mathbf{b}^{k+1}, \mathbf{z}^{k+1}, \mathbf{y}^k) \geq \frac{\rho h^3}{2} \|\mathbf{z}^k - \mathbf{z}^{k+1}\|^2.$$

Proof. From the optimality condition for (31) we conclude that \mathbf{z}^{k+1} satisfies

$$0 = \nabla g(\mathbf{z}^{k+1}) - \mathbf{y}^k - \rho h^3(\mathbf{b}^{k+1} - \mathbf{z}^{k+1}) = \nabla g(\mathbf{z}^{k+1}) - \rho h^3 \mathbf{y}^{k+1}$$

and therefore $\mathbf{y}^{k+1} = \nabla g(\mathbf{z}^{k+1})$. Similar to before, denoting $\mathcal{L}_\rho^k = \mathcal{L}_\rho(\mathbf{b}^{k+1}, \mathbf{z}^k, \mathbf{y}^k)$ and

$\mathcal{L}_\rho^{k+1} = \mathcal{L}_\rho(\mathbf{b}^{k+1}, \mathbf{z}^{k+1}, \mathbf{y}^k)$ we get

$$\begin{aligned} \mathcal{L}_\rho^k - \mathcal{L}_\rho^{k+1} &= g(\mathbf{z}^k) - g(\mathbf{z}^{k+1}) - (\mathbf{y}^k)^\top (\mathbf{z}^k - \mathbf{z}^{k+1}) + \frac{\rho h^3}{2} \left(\|\mathbf{b}^{k+1} - \mathbf{z}^k\|^2 - \|\mathbf{b}^{k+1} - \mathbf{z}^{k+1}\|^2 \right) \\ &= g(\mathbf{z}^k) - g(\mathbf{z}^{k+1}) - (\mathbf{y}^{k+1})^\top (\mathbf{z}^k - \mathbf{z}^{k+1}) + \frac{\rho h^3}{2} \|\mathbf{z}^k - \mathbf{z}^{k+1}\|^2 \\ &= g(\mathbf{z}^k) - g(\mathbf{z}^{k+1}) - \nabla g(\mathbf{z}^{k+1})^\top (\mathbf{z}^k - \mathbf{z}^{k+1}) + \frac{\rho h^3}{2} \|\mathbf{z}^k - \mathbf{z}^{k+1}\|^2 \\ &\geq \frac{\rho h^3}{2} \|\mathbf{z}^k - \mathbf{z}^{k+1}\|^2 \end{aligned}$$

where we used the convexity of g in the last step. ■

We now show an analogous result for the third ADMM step (32).

Lemma 9. *For any $\rho > 0$, the update $\mathbf{y}^k \rightarrow \mathbf{y}^{k+1}$ does not increase the value of the augmented Lagrangian, i.e.,*

$$\mathcal{L}_\rho(\mathbf{b}^{k+1}, \mathbf{z}^{k+1}, \mathbf{y}^k) - \mathcal{L}_\rho(\mathbf{b}^{k+1}, \mathbf{z}^{k+1}, \mathbf{y}^{k+1}) \geq 0.$$

Proof. Denoting $\mathcal{L}_\rho^k = \mathcal{L}_\rho(\mathbf{b}^{k+1}, \mathbf{z}^{k+1}, \mathbf{y}^k)$ and $\mathcal{L}_\rho^{k+1} = \mathcal{L}_\rho(\mathbf{b}^{k+1}, \mathbf{z}^{k+1}, \mathbf{y}^{k+1})$ we get

$$\mathcal{L}_\rho^k - \mathcal{L}_\rho^{k+1} = (\mathbf{y}^k - \mathbf{y}^{k+1})^\top (\mathbf{b}^{k+1} - \mathbf{z}^{k+1}) = \rho h^3 \|\mathbf{b}^{k+1} - \mathbf{z}^{k+1}\|^2 \geq 0. \quad \blacksquare$$

Having established the above results, we can now verify that our problem satisfies the three properties in [Theorem 5](#).

Proof of Theorem 5. We note that (P2), the sufficient decrease, follows immediately from [Lemmas 7 to 9](#) with $C_1 = \frac{\rho h^3}{2} - L_f > 0$.

(P1) The well-definedness of the updates $\mathbf{b}^k \rightarrow \mathbf{b}^{k+1}$ and $\mathbf{z}^k \rightarrow \mathbf{z}^{k+1}$ and thus also the update $\mathbf{y}^k \rightarrow \mathbf{y}^{k+1}$ follows from [Lemma 6](#). We next show that the sequence $\{\mathcal{L}(\mathbf{b}^k, \mathbf{z}^k, \mathbf{y}^k)\}_k$ is bounded below. First, note that for each k

$$f(\mathbf{b}^k) + g(\mathbf{b}^k) \geq 0.$$

Using that $\mathbf{y}^k = \nabla g(\mathbf{z}^k)$ for all k and the Lipschitz continuity of ∇g we note that

$$(42) \quad \|\mathbf{y}^{k+1} - \mathbf{y}^k\| \leq L_g \|\mathbf{z}^{k+1} - \mathbf{z}^k\|.$$

Combining this with $\rho h^3 \geq 2L_g$ we obtain

$$\begin{aligned} (43) \quad \mathcal{L}_\rho(\mathbf{b}^k, \mathbf{z}^k, \mathbf{y}^k) &= f(\mathbf{b}^k) + g(\mathbf{z}^k) + (\mathbf{y}^k)^\top (\mathbf{b}^k - \mathbf{z}^k) + \frac{\rho h^3}{2} \|\mathbf{b}^k - \mathbf{z}^k\|^2 \\ &= f(\mathbf{b}^k) + g(\mathbf{b}^k) + g(\mathbf{z}^k) - g(\mathbf{b}^k) - \nabla g(\mathbf{z}^k)^\top (\mathbf{z}^k - \mathbf{b}^k) + \frac{\rho h^3}{2} \|\mathbf{b}^k - \mathbf{z}^k\|^2 \\ &\geq f(\mathbf{b}^k) + g(\mathbf{b}^k) + \left(\frac{\rho h^3}{2} - L_g \right) \|\mathbf{b}^k - \mathbf{z}^k\|^2 \\ &\geq 0, \end{aligned}$$

which shows that $\{\mathcal{L}_\rho(\mathbf{b}^k, \mathbf{z}^k, \mathbf{y}^k)\}_k$ is lower bounded by zero. Finally, we need to show the boundedness of $\{\mathbf{b}^k, \mathbf{z}^k, \mathbf{y}^k\}$. For \mathbf{b}^k this directly follows from the boundedness of C . From (P2) we know that $\mathcal{L}_\rho(\mathbf{b}^k, \mathbf{z}^k, \mathbf{y}^k)$ is monotonically decreasing and therefore bounded above by $\mathcal{L}_\rho(\mathbf{b}^0, \mathbf{z}^0, \mathbf{y}^0)$. Using this, the boundedness of $\{\mathbf{b}^k\}$, (43), and the lower boundedness of $f(\mathbf{b}^k) + g(\mathbf{b}^k)$, we conclude the boundedness of $\{\mathbf{z}^k\}$. Finally, again using $\mathbf{y}^k = \nabla g(\mathbf{z}^k)$ and the Lipschitz continuity of ∇g , we have

$$\|\mathbf{y}^k\| = \|\nabla g(\mathbf{z}^k)\| \leq \|\nabla g(\mathbf{z}^k) - \nabla g(\mathbf{0})\| + \|\nabla g(\mathbf{0})\| \leq L_g \|\mathbf{z}^k\| + \|\nabla g(\mathbf{0})\|,$$

which shows the boundedness of $\{\mathbf{y}^k\}$.

(P3) We need to bound the derivatives of \mathcal{L}_ρ . First, we note that

$$\begin{aligned} \partial_{\mathbf{b}} \mathcal{L}_\rho(\mathbf{b}^{k+1}, \mathbf{z}^{k+1}, \mathbf{y}^{k+1}) &= \nabla f(\mathbf{b}^{k+1}) + \partial_{\nu_C}(\mathbf{b}^{k+1}) + \mathbf{y}^{k+1} + \rho h^3(\mathbf{b}^{k+1} - \mathbf{z}^{k+1}) \\ &= \nabla f(\mathbf{b}^{k+1}) + \partial_{\nu_C}(\mathbf{b}^{k+1}) + \mathbf{y}^k + \rho h^3(\mathbf{b}^{k+1} - \mathbf{z}^k) \\ &\quad + \mathbf{y}^{k+1} - \mathbf{y}^k + \rho h^3(\mathbf{z}^k - \mathbf{z}^{k+1}). \end{aligned}$$

The optimality condition of (30) implies that $\mathbf{0} \in f(\mathbf{b}^{k+1}) + \partial_{\nu_C}(\mathbf{b}^{k+1}) + \mathbf{y}^k + \rho h^3(\mathbf{b}^{k+1} - \mathbf{z}^k)$ and thus

$$\mathbf{y}^{k+1} - \mathbf{y}^k + \rho h^3(\mathbf{z}^k - \mathbf{z}^{k+1}) \in \partial_{\mathbf{b}} \mathcal{L}_\rho(\mathbf{b}^{k+1}, \mathbf{z}^{k+1}, \mathbf{y}^{k+1}),$$

which is bounded by $(L_g + \rho h^3) \|\mathbf{z}^k - \mathbf{z}^{k+1}\|$ due to (42). Second, we note that

$$\begin{aligned} \left\| \partial_{\mathbf{z}} \mathcal{L}_\rho(\mathbf{b}^{k+1}, \mathbf{z}^{k+1}, \mathbf{y}^{k+1}) \right\| &= \left\| \nabla g(\mathbf{z}^{k+1}) - \mathbf{y}^{k+1} - \rho h^3(\mathbf{b}^{k+1} - \mathbf{z}^{k+1}) \right\| \\ &= \left\| \mathbf{y}^k - \mathbf{y}^{k+1} \right\| \leq L_g \left\| \mathbf{z}^k - \mathbf{z}^{k+1} \right\|. \end{aligned}$$

Finally, we note that

$$\begin{aligned} \left\| \partial_{\mathbf{y}} \mathcal{L}_\rho(\mathbf{b}^{k+1}, \mathbf{z}^{k+1}, \mathbf{y}^{k+1}) \right\| &= \left\| \mathbf{b}^{k+1} - \mathbf{z}^{k+1} \right\| \\ &= \left\| \frac{1}{\rho h^3} (\mathbf{y}^{k+1} - \mathbf{y}^k) \right\| \leq \frac{L_g}{\rho h^3} \left\| \mathbf{z}^k - \mathbf{z}^{k+1} \right\|. \end{aligned}$$

Therefore, setting $C_2 = \max\{\frac{1}{2}, 3L_g\}$ there exists $\mathbf{d}^{k+1} \in \partial \mathcal{L}_\rho(\mathbf{b}^{k+1}, \mathbf{z}^{k+1}, \mathbf{y}^{k+1})$ as claimed. ■

Finally, we conclude by proving the main result, which is done exactly as in [38] by using the properties (P1)–(P3).

Proof of Theorem 4. In Theorem 5 we have established that the properties (P1)–(P3) hold for the iterates generated by (30)–(32), provided that $\rho > \frac{2}{h^3} \max\{L_f, L_g\}$. From (P1) we know that the set of iterates $\{\mathbf{b}^k, \mathbf{z}^k, \mathbf{y}^k\}$ is bounded, so it has a convergent subsequence. We denote a limit point by $(\mathbf{b}^*, \mathbf{z}^*, \mathbf{y}^*)$. Also from (P1) we know that the sequence $\{\mathcal{L}_\rho(\mathbf{b}^k, \mathbf{z}^k, \mathbf{y}^k)\}_k$ is bounded below. By (P2) it is also monotonically and sufficiently decreasing and this implies $\|\mathbf{b}^k - \mathbf{b}^{k+1}\| \rightarrow 0$ and $\|\mathbf{z}^k - \mathbf{z}^{k+1}\| \rightarrow 0$. Finally, by (P3), we get that there exists a subgradient $\mathbf{d}^k \in \partial \mathcal{L}_\rho(\mathbf{b}^k, \mathbf{z}^k, \mathbf{y}^k)$ with $\|\mathbf{d}^k\| \rightarrow 0$, which shows that $\mathbf{0} \in \partial \mathcal{L}_\rho(\mathbf{b}^*, \mathbf{z}^*, \mathbf{y}^*)$, and thus $(\mathbf{b}^*, \mathbf{z}^*, \mathbf{y}^*)$ is a stationary point. ■

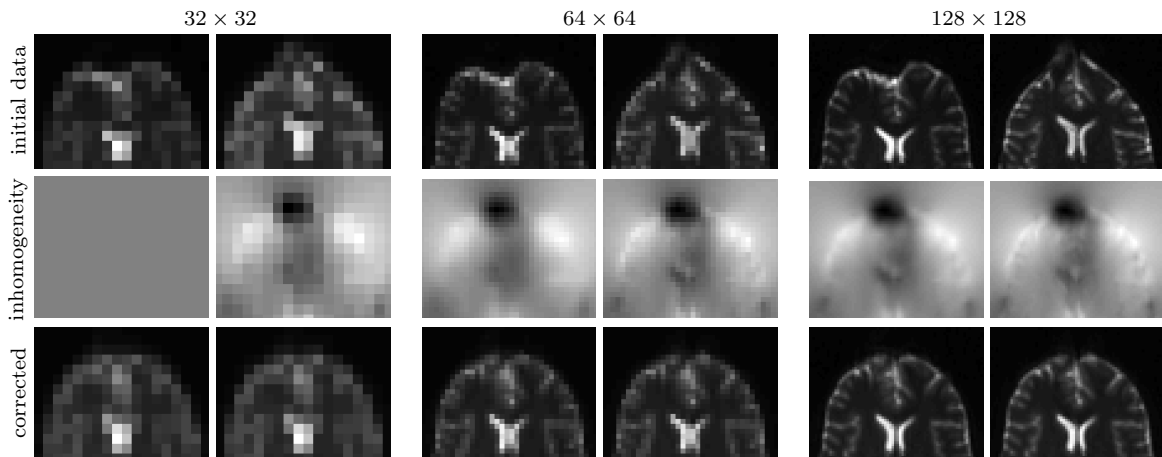


Figure 3. *Multilevel example. Deformed images \mathcal{I}_v and \mathcal{I}_{-v} (top row), estimated field inhomogeneity (middle row) and corrected images (bottom row) are visualized for three different discretization levels (coarse to fine from left to right). The image data is shown in pairs corresponding to the different phase encoding directions. The left plots for the field inhomogeneity visualize the starting guesses and the right plots the solutions on each level. Data is courtesy of Harald Kugel, University Hospital Münster, Germany, cf. section 5.*

The lower bound for ρ depends on the Lipschitz constants L_f and L_g of the distance and regularization function, respectively, as well as the voxel size h . The Lipschitz constants are commonly not available in practice. In our numerical experiments in section 5 we use a modified version of the adaptive augmentation parameter choice described in [2], which ensures that the augmentation parameter ρ remains larger than an experimentally defined lower bound ρ_{\min} , which we chose equal for all steps in the multilevel optimization. We compare this parameter choice method with a constant choice of the augmentation parameter and the unmodified adaptive scheme proposed for convex problems in [2].

4.4. Multilevel Strategy. As common in image registration and also suggested in [28], we employ a multilevel approach for solving (6); see [25] for details. In a nutshell, we start by solving a discrete version of (6) on a relatively coarse grid. Then, we prolongate the estimated field inhomogeneity to a finer grid to serve as a starting guess for the next discrete optimization problem. On each level, the resolution of the image data is increased as well and the procedure is repeated until the desired resolution is achieved. Apart from reducing computational costs on a coarse grid and obtaining excellent starting guesses, multilevel approaches have been observed to be more robust against local minima, which are less likely to occur in the coarse grid discretization; see Figure 3 for an example.

The incorporation of the Gauss-Newton method into this multilevel framework is straightforward, as the prolongation from a coarser grid can just be used as a starting guess for the Gauss-Newton iteration on a finer grid, as stated above.

For ADMM, however, there are several options how to initialize the optimization on a finer grid discretization, given the results on the coarser grid. We have tested and compared three strategies:

1. Prolongate all three coarse mesh vectors \mathbf{b}_c^{k+1} , \mathbf{z}_c^{k+1} , and \mathbf{u}_c^{k+1} and use the resulting

- fine mesh vectors \mathbf{b}_f , \mathbf{z}_f , and \mathbf{u}_f as initial guesses for the next level.
2. Restart ADMM using the fine mesh variable \mathbf{b}_f for both \mathbf{z}^0 and \mathbf{b}^0 and set the dual variable to zero, i.e., $\mathbf{u}^0 = \mathbf{0}$.
 3. Restart ADMM on the fine level using $\mathbf{b}^0 = \mathbf{z}^0 = \frac{1}{2}(\mathbf{b}_f + \mathbf{z}_f)$ and $\mathbf{u}^0 = \mathbf{0}$ as initial guesses.

In our examples, we obtained comparable results for all three strategies, however, the third strategy performed best and is used in the subsequent experiments.

5. Numerical Experiments. In this section, we perform numerical experiments to compare the effectiveness of the preconditioning techniques and the performance of the proposed ADMM method using real 2D and 3D data. We conclude the section by comparing the proposed methods to an existing state-of-the-art method for susceptibility artifact correction. A MacBook Pro laptop with 2.8 GHz Intel Core i7 processor and 16 GB 1600 MHz DD3 memory running MATLAB 2015A is used for all numerical experiments.

Test Data. The 2D data are courtesy of Harald Kugel, Department of Clinical Radiology, University Hospital Münster, Germany. A healthy subject was measured on a 3T scanner (Gyrosan Intera/Achieva 3.0T, System Release 2.5 (Philips, Best, NL)) using a standard clinical acquisition protocol. For this example we extracted one slice of a series of 2D spin echo EPI measurements that are performed using opposite phase encoding directions along the anterior posterior direction. The field of view is 240 mm \times 240 mm with a slice thickness of 3.6 mm. The acquisition matrix is 128 \times 128, resulting in a pixel size of 1.875 mm \times 1.875 mm and interpolated by zero filling to 0.9375 mm \times 0.9375 mm. Contrast parameters were TR = 9473 ms and TE = 95 ms. Here, we use a three-level multilevel strategy with grid sizes of 32 \times 32, 64 \times 64, and 128 \times 128.

The 3D data are provided by the Human Connectome Project [34]. We use a pair of unprocessed $b = 0$ weighted images of a female subject aged 31-35 (subject id 111312) acquired using reversed phase encoding direction on a 7T scanner. The field of view is 210 mm \times 210 mm \times 138.5 mm and the voxel size is 1.05 mm in all spatial directions. As in the 2D case, we use a three-level multilevel strategy using grid sizes of 50 \times 50 \times 33, 100 \times 100 \times 66, and 200 \times 200 \times 132.

Performance Of Preconditioners In 2D. We consider the Gauss-Newton-PCG method and investigate the performance of the preconditioners described in subsection 4.1. To allow for a direct comparison within reasonable time we consider the 2D test data described above. The main computational burden in GN-PCG is iteratively solving a linear system involving the approximate Hessian (17) in each Gauss-Newton iteration. Using PCG, the number of iterations required depends on the spectral properties of the preconditioned Hessian and in particular on the clustering of its eigenvalues.

The spectra of the approximated Hessian with and without preconditioning are illustrated in Figure 4 for the final Gauss-Newton iteration on the coarse level and parameters $\alpha = 200$, $\beta = 10$. It can be seen that all three preconditioners condense the spectrum around the eigenvalue 1. The tightest clustering is obtained using the symmetric Gauss-Seidel preconditioner, \mathbf{P}_{SGS} , that is, however, the most expensive and not easy to parallelize. The least effective preconditioner is the Jacobi preconditioner, \mathbf{P}_{Jac} , which is also the cheapest. A good trade-off between clustering of the eigenvalues and efficiency is observed for the proposed block-Jacobi

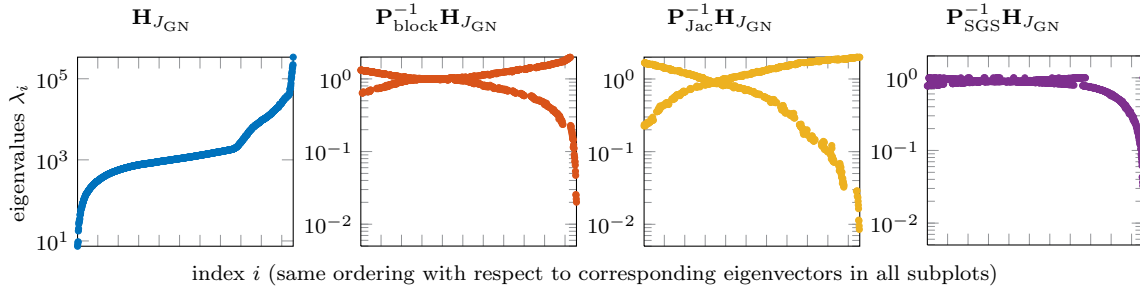


Figure 4. Spectra of the approximated Hessian (17) before and after applying the block-Jacobi, Jacobi, and symmetric Gauss-Seidel preconditioners described in subsection 4.1. As test data, we consider the final iteration on the coarse level of the 2D example also shown in Figure 3 with $\alpha = 200$ and $\beta = 10$.

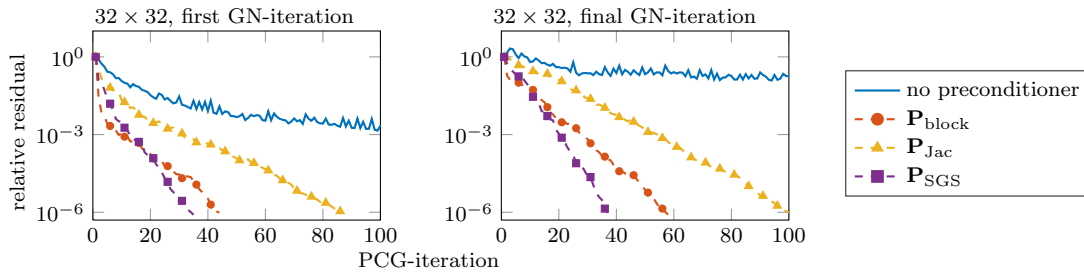


Figure 5. PCG performance for different preconditioning techniques in the first and final iteration of the coarse level of the 2D example also shown in Figure 3, where $\alpha = 200$, $\beta = 10$.

preconditioner $\mathbf{P}_{\text{block}}$.

We compare the performance of the PCG solver using the different preconditioners for the data from the coarse level of the 2D example in Figure 5. To illustrate the effect of the current estimate of \mathbf{b} on the convergence, we compare the performance of PCG in the first and final Gauss-Newton iteration. To demonstrate the convergence behavior, we approximately solve (18) to a relative residual tolerance of 10^{-6} . Note that during the Gauss-Newton algorithm, we use a relatively large tolerance of 10^{-1} . Comparing the subplots in Figure 5 it can be seen that the convergence is considerably faster in the first iteration, where $\mathbf{b} \equiv 0$, than in the final iteration. This effect is most pronounced for the unpreconditioned scheme but also notable for the preconditioned schemes. While the symmetric Gauss-Seidel preconditioner uses the smallest number of iterations overall, the proposed block-Jacobi preconditioner shows the best performance during the first few PCG-iterations. Therefore, and due to the fact that this solver is parallelizable and of low complexity, the block-Jacobi preconditioner is attractive for large-scale applications. Furthermore the symmetric Gauss-Seidel scheme has the highest computational cost per PCG-iteration (in both the first and final Gauss-Newton iteration), taking about 3.2 ms per PCG-iteration on average, whereas the block-Jacobi scheme only takes about 0.3 ms per PCG-iteration on average. The Jacobi scheme is the cheapest of the three preconditioners, taking only about 0.2 ms per PCG-iteration on average.

Finally, Figure 6 shows the condition number of the preconditioned approximate Hessian and the number of PCG-iterations required to achieve a relative residual tolerance of 10^{-1} in each Gauss-Newton iteration. Results for each level of the multilevel scheme with grid sizes

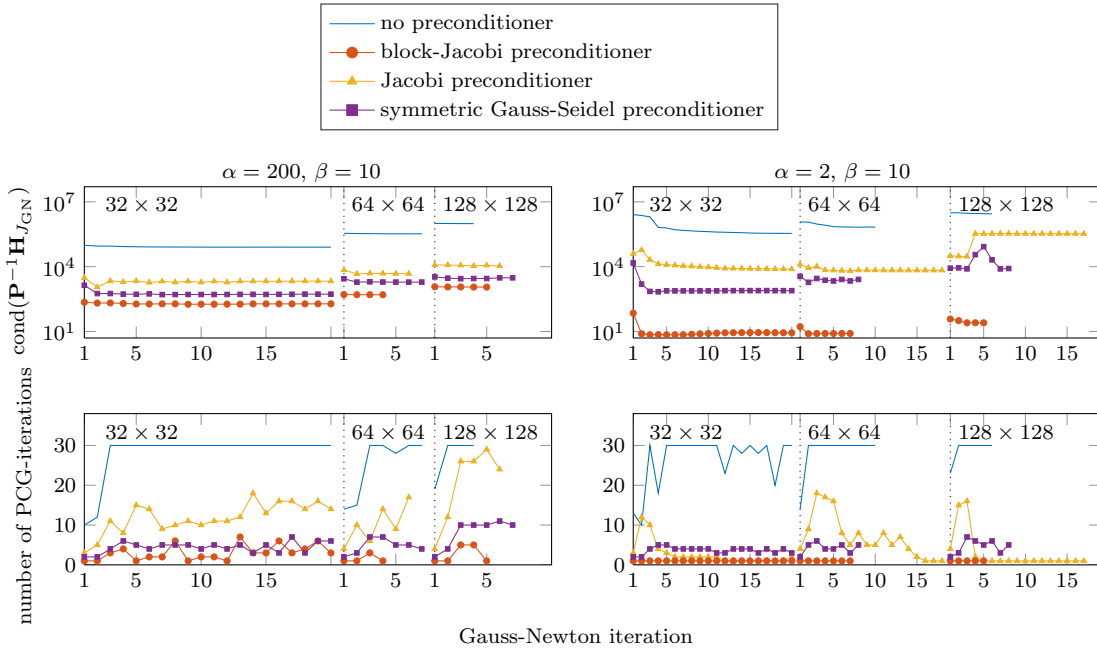


Figure 6. Condition number of preconditioned Hessian (17) and number of required PCG-iterations to achieve a relative residual tolerance of 10^{-1} for different options of preconditioners described in subsection 4.1. Results are shown for different discretization levels (divided by vertical dotted lines) using the 2D test data also shown in Figure 3 with $\alpha = 200, \beta = 10$ and $\alpha = 2, \beta = 10$ respectively.

of 32×32 , 64×64 , and 128×128 are shown. The penalty parameter is fixed at $\beta = 10$ but we consider two settings of the smoothness regularizer: $\alpha = 200$ and $\alpha = 2$. It can be seen that the block-Jacobi preconditioner outperforms the Jacobi preconditioner, while having only slightly higher computational cost per iteration. The total runtimes for the three-level optimization for the example with $\alpha = 200$ were 1.0 s without preconditioner, 0.7 s with the block-Jacobi, and 0.9 s with both the Jacobi and symmetric Gauss-Seidel preconditioners. In the case of $\alpha = 2$ the runtimes remain almost unchanged for all schemes except for the Jacobi preconditioner, where the runtime increases by a factor of about 1.8. This increase is due to the larger number of outer iterations.

Performance Of Preconditioners In 3D. We compare the performance of the different preconditioners for the 3D data set described above using $\alpha = 50$ and $\beta = 10$. Detailed convergence results are provided in Table 1. We show the decrease of the objective function value, the norm of the gradient and the number of PCG-iterations needed to solve (18) at each Gauss-Newton iteration. Here, the Gauss-Newton iterations $k = -1$ and $k = 0$ correspond to $\mathbf{b} = 0$ and the initial guess obtained by prolongation from the previous level, respectively. As in the previous example, the block-Jacobi preconditioner outperforms both the Jacobi and the symmetric Gauss-Seidel preconditioner. In many Gauss-Newton iterations only one or two PCG-iterations are needed. Furthermore the savings in computational cost per PCG-iteration when using the block-Jacobi instead of the symmetric Gauss-Seidel preconditioner are even more substantial in the 3D case. On the finest level, neither of the three methods satisfies the

Table 1

Convergence results for the 3D correction problem with $\alpha = 50$ and $\beta = 10$ for the different preconditioning strategies described in subsection 4.1. For each Gauss-Newton-iteration, we show the objective function value, the gradient norm, the number of PCG-iterations, and the relative residual of the PCG-solve. Empty rows indicate that the respective method has already converged with respect to the prescribed tolerances. On the finest level, all methods reach the maximum number of iterations without achieving the first condition in (24).

GN iter	Jacobi				symmetric Gauss-Seidel				block-Jacobi				
	J_{GN}	$\ \nabla J_{GN}\ $	iter	rel. res.	J_{GN}	$\ \nabla J_{GN}\ $	iter	rel. res.	J_{GN}	$\ \nabla J_{GN}\ $	iter	rel. res.	
50 × 50 × 33	-1	1.02e8	–	–	–	1.02e8	–	–	–	1.02e8	–	–	–
	0	1.02e8	3.49e6	–	–	1.02e8	3.49e6	–	–	1.02e8	3.49e6	–	–
	1	3.48e7	1.59e6	4	8.53e-2	3.21e7	1.53e6	2	8.72e-2	3.04e7	1.46e6	1	3.81e-2
	2	1.61e7	7.84e5	7	7.88e-2	1.47e7	7.48e5	3	8.81e-2	1.58e7	6.55e5	1	9.32e-2
	3	1.00e7	4.08e5	9	8.68e-2	9.30e6	3.87e5	4	7.69e-2	1.03e7	3.62e5	2	5.93e-2
	4	7.92e6	2.21e5	10	9.37e-2	7.60e6	2.05e5	4	9.59e-2	8.32e6	1.96e5	2	7.76e-2
	5	6.96e6	1.24e5	11	9.36e-2	6.89e6	1.13e5	5	7.06e-2	7.43e6	2.30e5	3	6.68e-2
	6	6.84e6	8.55e4	10	9.77e-2	6.72e6	4.47e4	4	9.13e-2	6.98e6	1.01e5	1	4.05e-2
	7	6.67e6	2.28e4	7	9.82e-2	6.67e6	4.26e4	6	8.21e-2	6.90e6	4.48e4	1	6.57e-2
	8	6.65e6	2.85e4	19	9.39e-2	6.66e6	3.52e4	4	7.96e-2	6.73e6	3.82e4	5	7.27e-2
9	6.64e6	2.17e4	16	9.73e-2	6.65e6	2.86e4	3	9.04e-2	6.72e6	3.13e4	1	8.80e-2	
10	6.63e6	1.89e4	15	9.62e-2	6.64e6	2.23e4	4	7.58e-2	6.72e6	4.33e4	2	9.84e-2	
100 × 100 × 66	-1	2.09e8	–	–	–	2.09e8	–	–	–	2.09e8	–	–	–
	0	5.20e7	1.94e6	–	–	5.20e7	1.95e6	–	–	5.22e7	1.95e6	–	–
	1	2.44e7	9.96e5	4	9.63e-2	2.35e7	9.95e5	2	6.94e-2	2.31e7	9.57e5	1	2.24e-2
	2	1.65e7	5.08e5	6	8.68e-2	1.93e7	7.53e5	2	9.07e-2	1.61e7	4.68e5	1	3.48e-2
	3	1.42e7	2.62e5	8	8.50e-2	1.49e7	3.85e5	3	6.41e-2	1.42e7	2.25e5	1	5.82e-2
	4	1.36e7	1.43e5	10	8.92e-2	1.42e7	2.93e5	3	8.02e-2	1.36e7	4.04e5	1	9.64e-2
	5	1.33e7	8.57e4	12	9.11e-2	1.35e7	1.54e5	3	8.92e-2	1.35e7	2.57e5	1	2.31e-2
	6	1.32e7	6.76e4	13	9.74e-2	1.35e7	1.34e5	4	9.94e-2	1.34e7	1.60e5	1	7.73e-2
	7	1.32e7	6.32e4	13	9.92e-2	1.33e7	7.97e4	4	8.63e-2	1.33e7	1.27e5	1	8.72e-2
	8	1.32e7	5.68e4	12	9.73e-2	1.32e7	7.61e4	5	8.13e-2				
9	1.31e7	5.18e4	13	9.15e-2	1.32e7	7.10e4	5	7.53e-2					
10					1.31e7	4.78e4	4	6.96e-2					
200 × 200 × 132	-1	3.35e8	–	–	–	3.35e8	–	–	–	3.35e8	–	–	–
	0	8.04e7	1.64e6	–	–	8.01e7	1.64e6	–	–	8.07e7	1.63e6	–	–
	1	6.86e7	1.45e6	6	8.93e-2	5.73e7	1.25e6	3	5.83e-2	6.85e7	1.44e6	1	2.11e-2
	2	5.95e7	1.28e6	6	9.40e-2	5.05e7	1.10e6	3	6.73e-2	5.91e7	1.27e6	1	2.24e-2
	3	5.24e7	1.13e6	6	9.98e-2	4.53e7	9.70e5	3	7.16e-2	5.54e7	1.19e6	1	2.40e-2
	4	4.69e7	9.91e5	7	8.88e-2	4.12e7	8.53e5	3	7.59e-2	4.90e7	1.05e6	1	2.48e-2
	5	4.26e7	8.71e5	7	9.36e-2	3.81e7	7.50e5	3	8.04e-2	4.41e7	9.16e5	1	2.66e-2
	6	3.93e7	7.66e5	7	1.00e-1	3.57e7	6.59e5	3	8.38e-2	4.04e7	8.02e5	1	2.87e-2
	7	3.66e7	6.74e5	8	9.19e-2	3.38e7	5.79e5	3	8.89e-2	3.75e7	7.02e5	1	3.13e-2
	8	3.46e7	5.92e5	8	9.74e-2	3.23e7	5.08e5	3	9.29e-2	3.53e7	6.13e5	1	3.39e-2
9	3.30e7	5.20e5	9	8.94e-2	3.12e7	4.47e5	3	9.64e-2	3.36e7	5.36e5	1	3.73e-2	
10	3.17e7	4.57e5	9	9.54e-2	2.95e7	7.01e6	4	7.21e-2	3.22e7	4.68e5	1	4.09e-2	

first stopping criterion (24) after 10 iterations, which is the default setting in HySCO [30]. In our experiments we found that increasing the number of iterations does not lead to considerable improvements of reconstruction quality. In total the block-Jacobi scheme takes 142 s, the Jacobi scheme takes 233 s, and the symmetric Gauss-Seidel scheme takes 316 s for the three-level optimization.

Performance Of ADMM. We study the performance of the proposed ADMM scheme and its dependence on the choice of the augmentation parameter ρ using the 3D data set described above. The convergence of the primal residual, dual residual, and ρ for the adaptive method, the fixed parameter method, and the adaptive method with lower bound, are visualized in

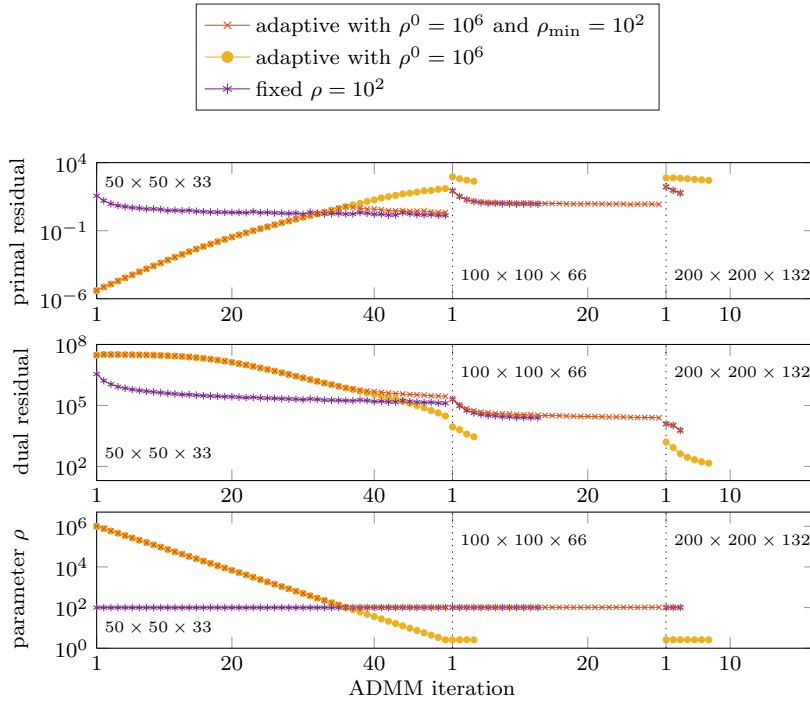


Figure 7. Convergence of ADMM for a multilevel 3D EPI susceptibility artifact correction. Two adaptive and one fixed strategies for choosing the augmentation parameter ρ in (29) are compared. First row shows the norm of the primal residual (cf. (40)) for each iteration of ADMM and each level in the coarse to fine hierarchy. Second row shows the norm of the dual residual (cf. (40)) and the bottom row shows the augmentation parameter for each iteration. The regularization parameter for the smoothing term is $\alpha = 50$.

Figure 7. In the fixed case we use $\rho = 10^2$, which is also the lower bound in the bounded adaptive method. For both adaptive schemes the initial parameter is $\rho^0 = 10^6$. As discussed in subsection 4.4, we average \mathbf{b} and \mathbf{z} after prolongation to start the next level. Clearly, larger values for ρ result in a smaller primal residual, whereas smaller values for ρ result in a smaller dual residual. The benefit of the adaptive method with lower bound is, that it forces the primal residual to converge fast during the first iterations and afterwards keeps the primal residual small while the dual residual converges as well. This way the equality constraint in (28) is almost satisfied during most iterations, meaning that we indeed solve the problem (28).

Note that, while ρ changes dramatically on the coarsest level, it remains constant on the finer levels, where computations are more costly. The separability of the first – and in our experience most expensive – ADMM subproblem (30) provides a way for substantial speed up by using parallel computing. In principle, the data of each image column can be processed completely in parallel. To strike a balance between communication overhead and computations, in our current MATLAB implementation we correct all image slices in parallel.

Comparison. We compare the quality of the proposed reconstruction methods to an established state-of-the-art method for susceptibility artifact correction. Exemplarily, we consider

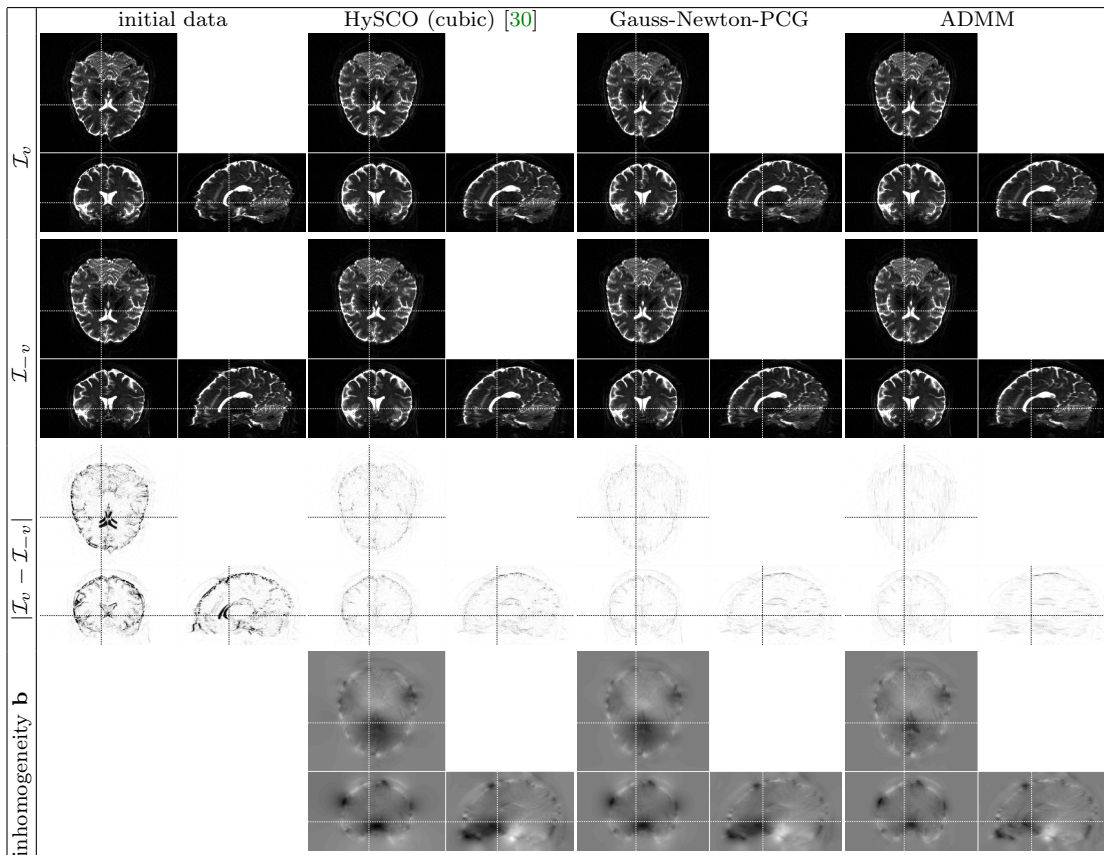


Figure 8. 3D correction results for high-resolution EPI-MRI brain data provided by the Human Connectome Project [34]. Initial data (left) and results of three reversed-gradient based correction methods are visualized using orthogonal slice views. The color axis are chosen identically in each row. First and second rows show initial data and corrected images for both phase-encoding directions. Third row shows the absolute difference between both images using an inverted color scale for improved visualization. A significant reduction of the image difference can be observed for all correction techniques. The bottom row shows the estimated field inhomogeneity that is comparable among all correction techniques.

HySCO [30] since it is based on the same variational formulation and uses the same three-level approach as our proposed method. In contrast to the proposed methods, HySCO uses a nodal discretization, which leads to coupling across slices and image columns (see second row in Figure 2), and provides only a simple Jacobi preconditioner. We use the same 3D data as in the previous section, visualize the correction results for all three different methods in Figure 8, and summarize quantitative results in Table 2. We provide results for two experiments using HySCO. First, we report results using the default settings in HySCO. By default, HySCO uses a smoothed cubic spline based approximation of the data described in [25], which aims at adding robustness. Since this comes at an additional computational costs, a second experiment using the same linear interpolation model used in the proposed methods is performed.

All methods effectively correct for susceptibility artifacts rendering the corrected image

Table 2

Comparison of the improvements in image similarity for different reversed-gradient methods applied to the 3D-MRI data with $\alpha = 50$ and $\beta = 10$ (in GN methods only). Image similarity between the initial and transformed blip-up and blip-down data is assessed using the sum of squared differences (SSD) distance [25] (smaller value associated with more similarity) and normalized cross-correlation (NCC) [25] (normalized to $[0, 1]$ where 1 is optimal).

	HySCO (cubic) [30]	HySCO (linear) [30]	Gauss-Newton-PCG	ADMM
SSD (\mathbf{b}^0)	$7.395 \cdot 10^{10}$	$7.395 \cdot 10^{10}$	$7.395 \cdot 10^{10}$	$7.395 \cdot 10^{10}$
SSD (\mathbf{b}^*)	$9.540 \cdot 10^9$	$1.557 \cdot 10^{10}$	$6.433 \cdot 10^9$	$5.058 \cdot 10^9$
reduction	87.1%	78.9%	91.3%	93.1%
NCC (\mathbf{b}^0)	0.529	0.529	0.529	0.529
NCC (\mathbf{b}^*)	0.924	0.879	0.955	0.964
runtime	2059 s	198 s	142 s	43 s

pairs visually more similar with both proposed methods slightly outperforming HySCO; see residual images in Figure 8 and Table 2. A notable difference is observed comparing the performance of HySCO with cubic B-spline and linear interpolation of the image data. While the former achieves a higher quality correction, the time-to-solution is around 34 minutes. With less than 3 minutes, the time-to-solution for the linear interpolation model is considerably lower, but it achieves considerably inferior correction results. Changing from the nodal discretization employed in HySCO to the face-staggered discretization proposed here, leads to a highly accurate correction (see improvement in image similarity), even with a linear interpolation model. As to be expected, the results for GN-PCG and ADMM yield almost identical results. The most striking difference between the different methods is the reduced time-to-solution. Both newly proposed methods outperform the existing approaches. In our comparison the fastest method is the parallelized implementation of ADMM, which yields a speedup factor of around 50x while the new GN-PCG yields a speedup factor of around 15x as compared to the default settings of HySCO.

6. Summary And Conclusion. In this paper, we present two efficient methods for susceptibility artifact correction of EPI-MRI. We consider a variational formulation of a reversed gradient based correction scheme similar to [28, 30, 17]. Our method requires one additional EPI-MRI acquisition with opposite phase-encoding direction and, thus, opposite distortion. We follow a discretize-then-optimize paradigm and propose a face-staggered discretization of the field inhomogeneity. This choice leads to a separable discrete distance function and constraints. While the overall optimization problem is, due to the smoothness regularizer, not separable we consider two optimization schemes that exploit the partially separable structure.

First, we propose a block-Jacobi preconditioner to be used in Gauss-Newton-PCG optimization schemes. The preconditioner is designed to exploit the respective block structure of the distance and penalty functions and also accounts for parts of the smoothness regularizer. The preconditioner is block-diagonal with tridiagonal structure and thus can be computed in parallel and with linear complexity. Using a 2D example, we demonstrate the improved clustering of eigenvalues as compared to the cheaper Jacobi preconditioner; see Figure 4. We also show the effectiveness of the block-Jacobi preconditioner for solving the Gauss-Newton system with very high accuracy; see Figure 6. Furthermore, we show that it considerably

reduces the number of PCG-iterations when used in combination with a GN-PCG using both a 2D and a 3D example; see [Figure 6](#) and [Table 1](#).

Second, we split the separable and non-separable parts of the objective function by adding an artificial variable and apply ADMM to compute a saddle-point of the associated augmented Lagrangian. The resulting subproblems can be solved efficiently. The first subproblem, albeit being non-convex, is separable and can be broken down into several smaller problems with only a few hundreds of unknowns that can be solved in parallel using sequential quadratic programming. The second subproblem consists of minimizing a convex quadratic with a block-diagonal Hessian with BTTB structure and, thus, can be solved efficiently and in parallel using DCTs. We provide a detailed convergence result that is similar to [38] but exploits the smoothness of our problem. We also derive a theoretical lower bound for the augmentation parameter in ADMM. Using a numerical experiment, we compare different adaption strategies for the augmentation parameter in [Figure 7](#). In our experience, adaptive choice of the parameter is possible, however, in view of the presented convergence result, we recommend using at least an empirically tuned lower bound to ensure convergence. We found that choosing a sufficiently large lower bound is critical to ensure smoothness of the solution.

The correction quality for both methods is comparable to state-of-the-art methods as shown using one example in [Figure 8](#). The most striking difference is the reduced time-to-solution for both methods. Using the proposed preconditioner in GN-PCG, runtime is reduced by a factor of around 15 in this example using a straightforward implementation in MATLAB. The implementation of GN-PCG is freely available as version 2 of HySCO as part of the ACID toolbox (<http://www.diffusiontools.com/documentation/hysco.html>).

A larger speedup factor of around 50 is achieved in our experiments using a relatively simple parallel implementation of the proposed ADMM method. Here, the separable structure of the computationally first, and most challenging, subproblem in ADMM is used by parallelizing over all image slices. Given our promising results, the ADMM method is an ideal candidate for implementation on massively parallel hardware such as Graphics Processing Units (GPU) and can be attractive for real-time applications such as [6].

7. Acknowledgements. We wish to thank Harald Kugel from the Department of Clinical Radiology, University Hospital Münster, Germany, for suggestions on a first draft of this manuscript and providing the 2D data used in our numerical experiments. The 3D data were provided by the Human Connectome Project, WU-Minn Consortium (Principal Investigators: David Van Essen and Kamil Ugurbil; 1U54MH091657) funded by the 16 NIH Institutes and Centers that support the NIH Blueprint for Neuroscience Research; and by the McDonnell Center for Systems Neuroscience at Washington University. We also like to thank Siawoosh Mohammadi, University Hospital Hamburg Eppendorf, Germany, for fruitful discussions and helpful advice.

REFERENCES

- [1] J. L. R. ANDERSSON, S. SKARE, AND J. ASHBURNER, *How to correct susceptibility distortions in spin-echo echo-planar images: application to diffusion tensor imaging*, *NeuroImage*, 20 (2003), pp. 870–888, doi:10.1016/S1053-8119(03)00336-7.
- [2] S. BOYD, N. PARIKH, E. CHU, B. PELEATO, AND J. ECKSTEIN, *Distributed Optimization and Statistical Learning via the Alternating Direction Method of Multipliers*, *Foundations and Trends® in Machine Learning*, 3 (2011), pp. 1–122, doi:10.1561/22000000016.

- [3] M. BURGER, J. MODERSITZKI, AND L. RUTHOTTO, *A hyperelastic regularization energy for image registration*, SIAM Journal on Scientific Computing, 35 (2013), pp. B132–B148, doi:10.1137/110835955.
- [4] P. CACHIER, E. BARDINET, D. DORMONT, X. PENNEC, AND N. AYACHE, *Iconic feature based nonrigid registration: the PASHA algorithm*, Computer Vision and Image Understanding, 89 (2003), pp. 272–298, doi:10.1016/S1077-3142(03)00002-X.
- [5] H. CHANG AND J. M. FITZPATRICK, *A Technique for Accurate Magnetic-Resonance-Imaging in the Presence of Field Inhomogeneities*, Medical Imaging, IEEE Transactions on, 11 (1992), pp. 319–329, doi:10.1109/42.158935.
- [6] P. DAGA, T. PENDSE, M. MODAT, M. WHITE, L. MANCINI, G. P. WINSTON, A. W. MCEVOY, J. THORNTON, T. YOUSRY, I. DROBNJAK, J. S. DUNCAN, AND S. OURSELIN, *Susceptibility artefact correction using dynamic graph cuts: Application to neurosurgery*, Medical Image Analysis, 18 (2014), pp. 1132–1142, doi:10.1016/j.media.2014.06.008.
- [7] J. C. DE MUNCK, R. BHAGWANDIEN, S. H. MULLER, F. C. VERSTER, AND M. B. VAN HERK, *The computation of MR image distortions caused by tissue susceptibility using the boundary element method*, Medical Imaging, IEEE Transactions on, 15 (1996), pp. 620–627, doi:10.1109/42.538939.
- [8] J. ECKSTEIN, *Augmented Lagrangian and alternating direction methods for convex optimization: A tutorial and some illustrative computational results*, RUTCOR Research Reports, Piscataway, NJ, 2012.
- [9] D. GABAY AND B. MERCIER, *A dual algorithm for the solution of nonlinear variational problems via finite element approximation*, Computers & Mathematics with Applications, 2 (1976), pp. 17–40, doi:10.1016/0898-1221(76)90003-1.
- [10] R. GLOWINSKI, *On Alternating Direction Methods of Multipliers: A Historical Perspective*, in Modeling, Simulation and Optimization for Science and Technology, Springer Netherlands, Dordrecht, 2014, pp. 59–82, doi:10.1007/978-94-017-9054-3_4.
- [11] G. H. GOLUB, M. HEATH, AND G. WAHBA, *Generalized cross-validation as a method for choosing a good ridge parameter*, Technometrics, 21 (1979), pp. 215–223, doi:10.1080/00401706.1979.10489751.
- [12] E. HABER AND D. OLDENBURG, *A GCV based method for nonlinear ill-posed problems*, Computational Geosciences, 4 (2000), pp. 41–63, doi:10.1023/A:1011599530422.
- [13] S. HAKER, L. ZHU, A. TANNENBAUM, AND S. ANGENENT, *Optimal Mass Transport for Registration and Warping*, International Journal of Computer Vision, 60 (2004), pp. 225–240, doi:10.1023/B:VISI.0000036836.66311.97.
- [14] P. C. HANSEN, *Rank-deficient and discrete ill-posed problems*, SIAM Monographs on Mathematical Modeling and Computation, Society for Industrial and Applied Mathematics (SIAM), Philadelphia, PA, 1998, doi:10.1137/1.9780898719697.
- [15] P. C. HANSEN, J. G. NAGY, AND D. P. O’LEARY, *Deblurring Images: Matrices, Spectra and Filtering*, Matrices, Spectra, and Filtering, Society for Industrial and Applied Mathematics (SIAM), Philadelphia, PA, 2006, doi:10.1137/1.9780898718874.
- [16] M. R. HESTENES AND E. STIEFEL, *Methods of Conjugate Gradients for Solving Linear Systems*, Journal of Research of the National Bureau of Standards, 49 (1952), pp. 409–436.
- [17] D. HOLLAND, J. M. KUPERMAN, AND A. M. DALE, *Efficient correction of inhomogeneous static magnetic field-induced distortion in Echo Planar Imaging*, NeuroImage, 50 (2010), pp. 175–183, doi:10.1016/j.neuroimage.2009.11.044.
- [18] X. HONG, X. V. TO, I. TEH, J. R. SOH, AND K.-H. CHUANG, *Evaluation of EPI distortion correction methods for quantitative MRI of the brain at high magnetic field*, Magnetic Resonance Imaging, 33 (2015), pp. 1098–1105, doi:10.1016/j.mri.2015.06.010.
- [19] M. O. IRFANOGLU, P. MODI, A. NAYAK, E. B. HUTCHINSON, J. SARLLS, AND C. PIERPAOLI, *DR-BUDDI (Diffeomorphic Registration for Blip-Up blip-Down Diffusion Imaging) method for correcting echo planar imaging distortions*, NeuroImage, 106 (2015), pp. 284–299, doi:10.1016/j.neuroimage.2014.11.042.
- [20] P. JEZZARD, *Correction of geometric distortion in fMRI data*, NeuroImage, 62 (2012), pp. 648–651, doi:10.1016/j.neuroimage.2011.09.010.
- [21] P. JEZZARD AND R. S. BALABAN, *Correction for geometric distortion in echo planar images from B0 field variations.*, Magnetic Resonance in Medicine, 34 (1995), pp. 65–73, <http://eutils.ncbi.nlm.nih.gov/entrez/eutils/eflink.fcgi?dbfrom=pubmed&id=7674900&retmode=ref&cmd=prlinks>.
- [22] D. LE BIHAN, J. F. MANGIN, C. POUPON, C. A. CLARK, S. PAPPATA, N. MOLKO, AND H. CHABRIAT, *Diffusion tensor imaging: Concepts and applications*, Journal of Magnetic Resonance Imaging,

- 13 (2001), pp. 534–546, <http://eutils.ncbi.nlm.nih.gov/entrez/eutils/elink.fcgi?dbfrom=pubmed&id=11276097&retmode=ref&cmd=prlinks>.
- [23] V. I. MADAI, S. Z. MARTIN, F. C. VON SAMSON-HIMMELSTJERNA, C. X. HERZIG, M. A. MUTKE, C. N. WOOD, T. THAMM, S. ZWEYNERT, M. BAUER, S. HETZER, M. GÜNTHER, AND J. SOBESKY, *Correction for Susceptibility Distortions Increases the Performance of Arterial Spin Labeling in Patients with Cerebrovascular Disease*, *Journal of Neuroimaging*, (2016), doi:10.1111/jon.12331.
- [24] A. MANG AND G. BIROS, *An Inexact Newton–Krylov Algorithm for Constrained Diffeomorphic Image Registration*, *SIAM Journal on Imaging Sciences*, 8 (2015), pp. 1030–1069, doi:10.1137/140984002.
- [25] J. MODERSITZKI, *FAIR: flexible algorithms for image registration*, vol. 6 of *Fundamentals of Algorithms*, Society for Industrial and Applied Mathematics (SIAM), Philadelphia, PA, 2009, doi:10.1137/1.9780898718843.
- [26] J. NOCEDAL AND S. WRIGHT, *Numerical Optimization*, Springer Series in Operations Research and Financial Engineering, Springer Science & Business Media, New York, NY, 2006, doi:10.1007/978-0-387-40065-5.
- [27] R. T. ROCKAFELLER AND J.-B. W. ROGER, *Variational Analysis*, vol. 317 of *Grundlehren der mathematischen Wissenschaft*, Springer-Verlag Berlin Heidelberg, Berlin, 1998, (3rd printing 2009), doi:10.1007/978-0-387-40065-5.
- [28] L. RUTHOTTO, H. KUGEL, J. OLESCH, B. FISCHER, J. MODERSITZKI, M. BURGER, AND C. H. WOLTERS, *Diffeomorphic susceptibility artifact correction of diffusion-weighted magnetic resonance images*, *Physics in Medicine and Biology*, 57 (2012), pp. 5715–5731, doi:10.1088/0031-9155/57/18/5715.
- [29] L. RUTHOTTO AND J. MODERSITZKI, *Non-linear Image Registration*, in *Handbook of Mathematical Methods in Imaging*, Springer New York, New York, NY, 2015, pp. 2005–2051, doi:10.1007/978-1-4939-0790-8_39, http://link.springer.com/referenceworkentry/10.1007/978-1-4939-0790-8_39/fulltext.html.
- [30] L. RUTHOTTO, S. MOHAMMADI, C. HECK, AND W. N. MODERSITZKI, J., *Hyperelastic Susceptibility Artifact Correction of DTI in SPM*, *Bildverarbeitung für die Medizin*, (2013), doi:10.1007/978-3-642-36480-8_60.
- [31] Y. SAAD, *Iterative Methods for Sparse Linear Systems*, Second Edition, Society for Industrial and Applied Mathematics (SIAM), Philadelphia, PA, 2003.
- [32] S. SKARE AND J. L. R. ANDERSSON, *Correction of MR image distortions induced by metallic objects using a 3D cubic B-spline basis set: Application to stereotactic surgical planning*, *Magnetic Resonance in Medicine*, 54 (2005), pp. 169–181, doi:10.1002/mrm.20528.
- [33] M. K. STEHLING, R. TURNER, AND P. MANSFIELD, *Echo-Planar Imaging - Magnetic-Resonance-Imaging in a Fraction of a Second*, *Science*, 254 (1991), pp. 43–50, <http://eutils.ncbi.nlm.nih.gov/entrez/eutils/elink.fcgi?dbfrom=pubmed&id=1925560&retmode=ref&cmd=prlinks>.
- [34] D. C. VAN ESSEN, K. UGURBIL, E. AUERBACH, D. BARCH, T. E. J. BEHRENS, R. BUCHOLZ, A. CHANG, L. CHEN, M. CORBETTA, S. W. CURTISS, S. DELLA PENNA, D. FEINBERG, M. F. GLASSER, N. HAREL, A. C. HEATH, L. LARSON-PRIOR, D. MARCUS, G. MICHALAREAS, S. MOELLER, R. OOSTENVELD, S. E. PETERSEN, F. PRIOR, B. L. SCHLAGGAR, S. M. SMITH, A. Z. SNYDER, J. XU, E. YACOUB, AND W.-M. H. CONSORTIUM, *The Human Connectome Project: A data acquisition perspective*, *NeuroImage*, 62 (2012), pp. 2222–2231, doi:10.1016/j.neuroimage.2012.02.018.
- [35] J. VARDAL, R. A. SALO, C. LARSSON, A. M. DALE, D. HOLLAND, I. R. GROOTE, AND A. BJØRNERUD, *Correction of B₀-Distortions in Echo-Planar-Imaging-Based Perfusion-Weighted MRI*, *Journal of Magnetic Resonance Imaging*, 39 (2013), pp. 722–728, doi:10.1002/jmri.24213.
- [36] T. VERCAUTEREN, X. PENNEC, A. PERCHANT, AND N. AYACHE, *Diffeomorphic demons: Efficient non-parametric image registration*, *NeuroImage*, 45 (2009), pp. 61–72, doi:10.1016/j.neuroimage.2008.10.040.
- [37] C. R. VOGEL, *Computational Methods for Inverse Problems*, Society for Industrial and Applied Mathematics (SIAM), Philadelphia, PA, Philadelphia, PA, 2002, doi:10.1137/1.9780898717570.
- [38] Y. WANG, W. YIN, AND J. ZENG, *Global Convergence of ADMM in Nonconvex Nonsmooth Optimization*, *arXiv.org*, (2015), <http://arxiv.org/abs/1511.06324v3>, arXiv:1511.06324v3 [math.OC].